Charles University

Faculty of Science

Study program: Chemistry

Branch of study: Physical chemistry

Bc. Daniel Mildner

The preparation of functionalized nonplanar aromatics and study of their physical properties at nanoscale

Příprava funkcionalizovaných neplanárních aromátů a studium jejich fyzikálních vlastností v nanoměřítku

Master thesis

Supervisor: RNDr. Ivo Starý, CSc.

Prague, 2021

Acknowledgment

In the first place, let me thank my supervisor Dr. Ivo Starý for giving me unlimited trust and independence while working on my project in his laboratory. I also very much appreciate Dr. Irena G. Stará for offering me worthy opportunities for professional development. I am extremely grateful to Dr. Jiří Rybáček for helpful guidance and priceless advice when making decisions. Further, I acknowledge Dr. Jaroslav Vacek and Dr. Ladislav Sieger for useful consultations.

I would like to extend my sincere thanks to Dr. Jindřich Nejedlý for his endless devotion, experience, and calm and cheerful approach to solving problems. Then, I am thankful to Mgr. Václav Houska, Dr. Isabel Gay Sánchez, Ing. Jan Hanus, and Mgr. Jiří Klívar for sharing practical advice and support. Special thanks should go to Dr. Andrej Jančařík, who laid the foundation for the synthesis used in this work. I also thank Martin McLaughlin for a preparation of a tetrayne starting synthetic block.

I would like to recognize Dr. Radek Pohl for NMR assignment, Dr. Ivana Císařová for X-ray diffraction experiments, Dr. Lucie Bednárová for measuring UV, fluorescence, and ECD spectra, Ing. Pavel Fiedler for IR experiments and mass spectrometry and analytical departments for their services.

Finally, I am thankful to my parents for their never-ending support not only in my studies.

This work was supported by the Czech Science Foundation (Reg. No. 20-23566S) and the Institute of Organic Chemistry and Biochemistry CAS (RVO: 61388963).

Declaration:

Hereby, I declare, that I wrote the *Thesis* independently and that I cited all sources and co-authors. Neither this work, nor its any part, was used to obtain any other or identical academic degree.

In Prague on August 7, 2021

signature

Prohlášení:

Prohlašuji, že jsem závěrečnou práci zpracoval samostatně a že jsem uvedl všechny použité informační zdroje a spoluautory. Tato práce ani její podstatná část nebyla předložena k získání jiného nebo stejného akademického titulu.

V Praze dne 7. srpna 2021

podpis

Abstract

The *Thesis* studies single-molecule conductance of helicenes by means of scanning tunneling microscopy-based break-junction (STM-BJ) device. Particularly, it focuses on a question how the conductance of helicenes changes with the increased number of aromatic rings.

Firstly, *Introduction* about helicenes is given, namely their syntheses, properties, and applications. Further, methods of single molecule analysis, namely scanning tunneling microscope and break-junction techniques, are discussed with emphasis on organic molecules and their conductance.

In the next part, *Results and discussion,* the synthesis of helicenes is presented and their single-molecule conductance is studied. Through STM-BJ measurements, decreasing trend in molecular conductance with increasing length of a molecular wire is proved. Above that, the correlation of experimental data with theoretical calculations and X-ray diffraction experiments confirms that a single-molecule conductance is measured.

Finally, the *Experimental section* provides detailed description of experimental procedures both for organic and physical experiments.

Abstrakt

Tato *práce* se zabývá měřením vodivosti helicenů na úrovni jednotlivých molekul pomocí break-junction metody založené na principu rastrovacího tunelovacího mikroskopu (STM-BJ z angl. Scanning Tunneling Microscopy-based Break-Junction). Zvláštní důraz je kladen na otázku, jak se mění vodivost helicenů se vzrůstajícím počtem aromatických jader.

Nejprve jsou v *teoretickém úvodu* shrnuty informace o helicenech, jejich přípravě, vlastnostech a aplikacích. Dále jsou diskutovány metody studia látek na úrovni jednotlivých molekul, jmenovitě použití principů rastrovacího tunelovacího mikroskopu a break-junction techniky, se zaměřením na organické molekuly a jejich vodivosti.

Ve *výsledcích* je představena syntéza helicenů a měření jejich vodivostí. Pomocí STM-BJ metody byl potvrzen obecný trend klesající vodivosti pro vzrůstající délku molekul. Srovnání experimentálních dat s teoretickými výpočty a výsledky z rentgenové difrakce potvrzuje, že naměřené vodivosti odpovídají jedné molekule.

Experimentální část obsahuje detailní popisy jak organických, tak fyzikálních experimentů.

List of contents

1 Theoretical background

1.1 Helicenes

Helicenes are a class of polyaromatic hydrocarbons with all-*ortho*-annulated aromatic rings (Fig. 1a). To release steric repulsion between the ends of a molecule, the helicene leaves its planar geometry, favored for aromatic compounds, and forms a helix. Compounds as small as phenanthrene exhibit the distortion upon substitution in the "fjord" region.[1] Although not planar, helicenes are more stable than their linear counterparts, acenes (Fig. 1b) since there are more Clar's sextets (colored in red in Fig. 1) on a helicene molecule.[2] They are also more soluble than acenes because the distortion makes them less prone to intermolecular π-π stacking.

Newman and Lednicer published the nomenclature system for helicenes in 1956.[3] For helicene with *n* aromatic rings, they proposed a notation [*n*]helicene or to express the number of rings by greek prefixes *penta*-, *hexa*-, *hepta*- *etc*. They were first to intentionally prepare a helicene when they synthetized [6]helicene **1** (Fig. 1a) from 2 naphthyl blocks and resolved it into enantiomers by crystallization with a chiral agent.

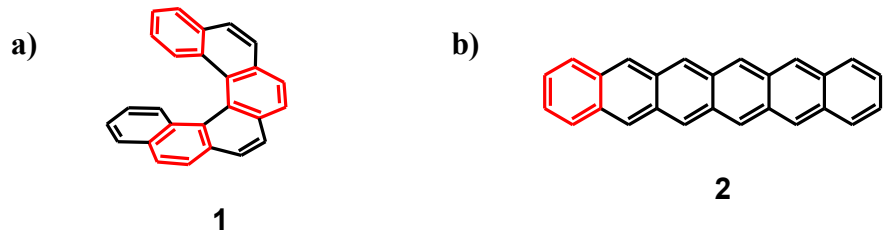

Fig. 1: a) Structure of [6]helicene **1** and b) its linear analogue hexacene **2** showing 3 Clar's sextets (red) for helicene **1** compared to 1 for acene **2**.

Thanks to their helical shape, helicenes are inherently chiral, *i.e.*, chiral even without any stereogenic center present. Therefore, two enantiomers can exist denoted with stereodescriptors *P* for dextrorotatory, and *M* for levorotatory enantiomer (Fig. 2). Helicenes in their optically pure form show extremely large values of specific optical rotation up to thousands deg·mL·g^{-1}·dm^{-1}.[4] They usually exhibit intense Cotton effect in their electronic circular dichroism (ECD) spectra, which is used for assigning the absolute configuration of enantiomers. There is an empirical rule reading, if the sign of the longest wavelength band is

positive (or negative), the helicity is *P* (or *M*). Both specific optical rotation and ECD spectra can be calculated theoretically.

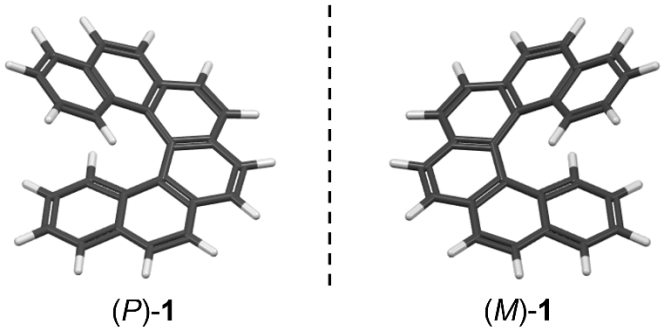

Fig. 2: Structures of *P* and *M* enantiomers of [6]helicene **1**.

Generally, helicenes are chemically inert compounds, which do not react with common acids or bases, and are not affected by most of the oxidizing, nor reducing agents. As fully aromatic hydrocarbons, they absorb radiation in UV region and some helicenes fluoresce.[5] The energy of both absorption and emission is typically shifted to lower values for increasing number of aromatic rings in molecular backbone of helicene. Thanks to their ability to absorb UV radiation and fluoresce together with their non-linear optical properties, they have been envisaged for future application in optical devices such as circularly polarized organic light-emitting diodes[6] and, for example, a transistor-based sensor for circularly polarized light using helicenes in an active layer has already been published.[7] Beside organic electronics, helicenes are studied in fields like enantioselective catalysis,[8] liquid crystals,[9] chiral recognition,[10] and spintronics.[11]

Although helicenes are thermally stable compounds, their enantiomers undergo thermal racemization in solution. The racemization proceeds at room temperature for [5]helicene but elevated temperature is needed for [*n*]helicenes with $n > 5$.[12] The process is described by the reversible first-order kinetics, and it is solely conformational process.

The helicene structure can be varied. Heterohelicenes contain heteroatoms in their structure leading to aza-, oxa- or thiahelicenes (Fig. 3a). Cationic azahelicenes, called helquats, were studied with respect to their redox properties, where, for example, [5]helquat **4** (Fig. 3b) could undergo two one-electron reduction steps to form a neutral product.[13] Other structurally similar compounds are heliphenes (Fig. 3c), helical oligophenylenes. Both helicenes

and heliphenes could be prepared *via* [2+2+2] cyclotrimerization, though the yields for heliphenes were rather low.[14,15]

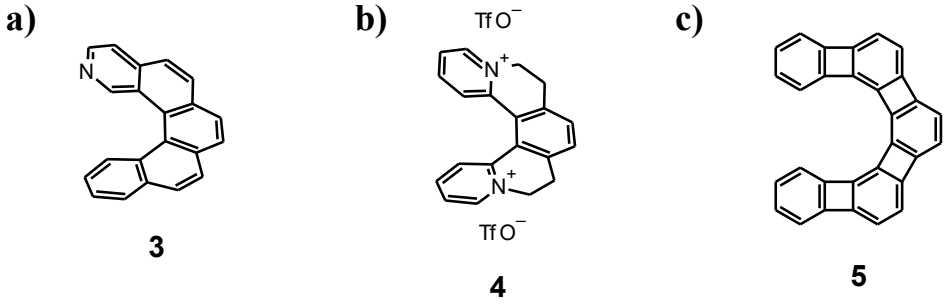

Fig. 3: Exemplary structures of a) 2-aza[5]helicene **3**, b) [5]helquat **4**, and c) [5]heliphene **5**.

1.2 Helicene synthesis

Various synthetic approaches have been developed since the first preparation of azahelicene by Meisenheimer and co-workers in 1903.[16] Helicenes have been prepared, for example, by Friedel-Crafts-type reactions[17] or Diels-Alder reaction.[18] In 1960s, photocyclodehydrogenation of stilbenes was introduced as another synthetic route to helicenes (Scheme 1).[19] Since then, it became the most predominant method to synthesize helicenes[20] because the precursors are easy to prepare and a multiple reaction is also possible.[21]

Scheme 1

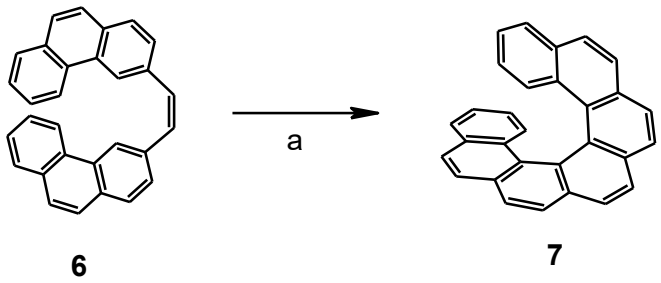

a) I_2, benzene, RT, Hg lamp, 8 h, 13 %

Basically, photocyclodehydrogenation reaction is based on a UV-initiated pericyclic reaction followed by an oxidative dehydrogenation. However, the UV radiation can trigger also an alternative reaction pathway on stilbenes, [2+2] cycloaddition.[22] Consequently, stilbene must be used in a low concentration, what limits the reaction scale-up. Although there are other

issues like a regioselectivity control,[23] even long helicenes up to [16]helicene were prepared by this method.[24]

Another important milestone in helicene synthesis was introduction of [2+2+2] cyclotrimerization of oligoalkynes by Starý and Stará in 1998.[25] The reaction is mediated by transition metal complexes based on Co, Ni or Rh. It proceeds mostly intramolecularly and so three aromatic rings get created in one synthetic step. The energy released from aromatization determines then a highly exergonic character of the reaction.[26] Beside triynes, nitriles and even dinitriles undergo cyclotrimerization and give azahelicenes or diazines,[27] but the energy gain is not as high as for alkynes.

Scheme 2

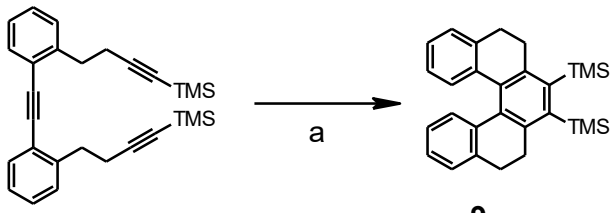

8 **9**

a) $CpCo(CO)_2$ (40 mol%), PPh_3 (80 mol%), decane, 140 °C, halogen lamp, 2.5 h, 71 %

The first cyclotrimerization experiments, which led to the partially saturated tetrahydro[5]helicenes,[25] relied on triynes with two triple bonds attached to aromatic rings by a saturated alkane tether (Scheme 2). Fully aromatic helicenes were then prepared by oxidation of hydrohelicenes with DDQ.[28] Another possibility was to start directly from *cis*,*cis*-dienetriynes[29] analogous to triyne **8**, which have the two triple bonds attached by ethylene linkers (Scheme 3, method a). However, the dienetriynes are chemically unstable and, therefore, a different approach, where the double bonds are incorporated into aromatic rings, has been designed (Scheme 3, method b). Indeed, such improved starting materials are stable and easily accessible through coupling reactions in high yields.[30]

Scheme 3

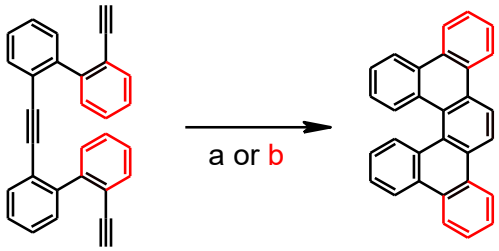

10 **11**

a) $Ni(cod)_2$ (1.0 eq.), THF, RT, 15 min, 83 % (red parts omitted)
b) $Ni(cod)_2$ (20 mol%), PPh_3 (40 mol%), THF, RT, 10 min, 96 % (red parts involved)

1.3 Scanning tunneling microscopy

Development of scanning tunneling microscopy (STM) enabled imaging single molecules deposited on a conducting surface by scanning it with a nanosized metallic tip (Fig. 4). The electric tunneling current between the tip and the surface is measured and once assigned to position on the substrate surface, it can serve for the image construction. The STM surface analysis is used by physicists in semiconductor or thin film research. Chemistry was also adapted to STM, so products of chemical reactions can be analyzed on metal surfaces.

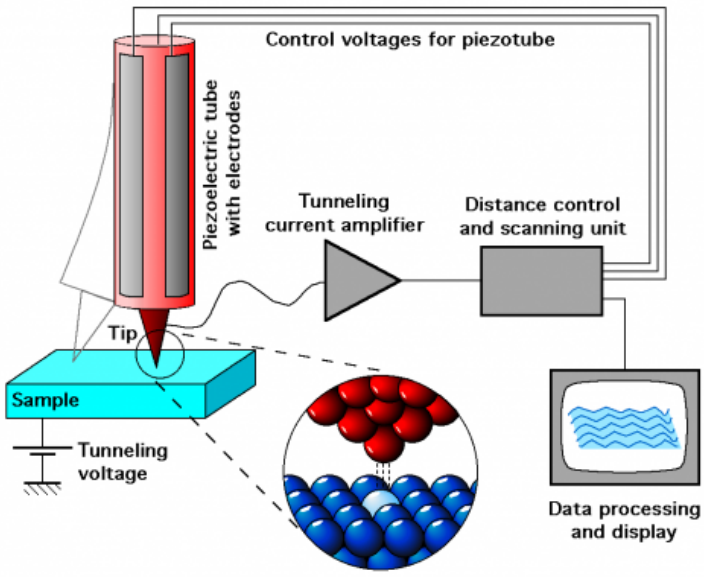

Fig. 4: Scheme of STM instrumentation with a magnified tip-substrate interface (© Michael Schmid, TU Wien[31]).

The first STM device was constructed by Young in 1972.[32] The tip movement was controlled by a piezoelectric actuator, what persisted until today. Anyway, the author did not achieve the fullest resolution because of insufficient insulation from vibrations. This problem was solved in 1981 by Binnig and Rohrer[33] from IBM Research lab in Zurich, who further developed this method and obtained images even with atomic resolution (Fig. 5).[34] In 1986, they were awarded the Nobel Prize in physics "*for their design of the scanning tunneling microscope.*"[35]

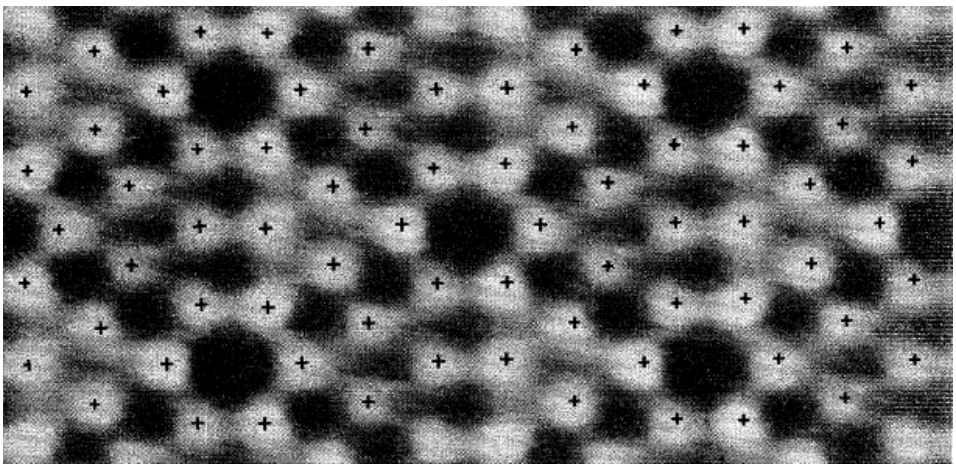

Fig. 5: STM image of Si(111) surface with 7 x 7 representation (adapted from ref. 34).

The working principle of STM is based on the tunneling effect, a quantum mechanical phenomenon, which gives the particle a nonzero transmission probability to overcome a potential barrier of a finite height. The tunneling current *I* between the two metallic electrodes decays exponentially with the height of the barrier *s* (Eq. 1).[36]

$$I = UA(U)\exp\left(-2s\sqrt{\frac{2m\varphi}{\hbar^2}}\right) \quad (1)$$

Here, the bias voltage is represented by *U*, *A(U)* accounts for the voltage dependent influence of the electron structure of the tip and the sample, *m* is the effective mass of a particle (electron), φ stands for the height of the potential barrier (metal work function), and ħ is a reduced Planck's constant.

STM works basically in two operational modes. In a constant height mode, the tip moves in a horizontal plane parallel to the surface and the current amplitude is used for the image

construction. However, only flat surfaces can be analyzed by this method. The limitation is overcome by a constant current mode, where electric current is preserved at a particular reference level by a feedback loop. Actual current magnitude is compared with the reference value and their difference determines the change of input voltage applied to a piezo actuator. The incremental changes in voltage are used to construct the final image.

A regular STM microscope operates at ambient conditions and can display objects as small as nanometres in size.[37] Anyway, it is the ultra-high vacuum STM (UHV STM) devices which routinely achieve submolecular resolution. An example of STM image (Fig. 6a) shows a 2D array of molecules **12** (Fig. 6b).[38] Ambient STM is much simpler in instrumentation and can be adjusted to scanning tunneling microscopy-based break-junction (STM-BJ) device. STM-BJ technique statistically measures the tunneling current through a molecule to obtain its conductance.

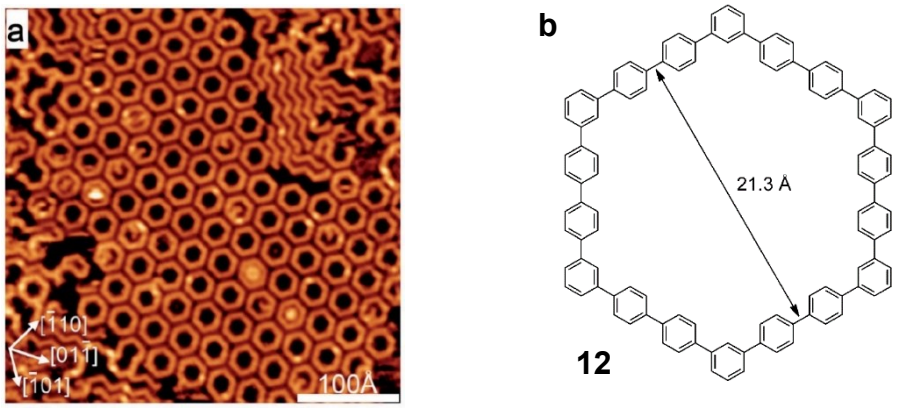

Fig. 6: a) Overview constant-current UHV STM image of 2D array of molecules **12** on Cu(111) with the depicted crystallographic directions (adapted from ref. 38) and b) structure of **12** with the depicted molecular length.

1.4 Scanning tunneling microscopy-based break-junction

In a break-junction (BJ) mode, STM repeatedly pushes the metallic tip into the substrate surface and pulls it back. When the junction breaks, atomically thin electrodes are formed and if the surface is covered with organic compound, a molecule can get trapped between

the electrodes. When bias voltage is applied, conductance through a single molecule can be measured (Fig. 7).

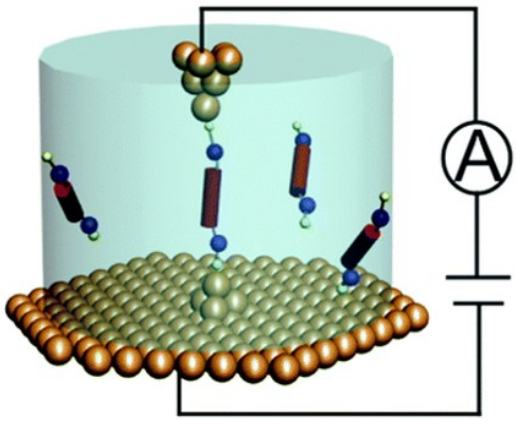

Fig. 7: STM-BJ setup scheme (adapted from ref. 39).

Electrical conductance at a macroscopic level is governed by Ohm's law, which is a consequence of electron inelastic scattering by impurities or lattice defects. Anyway, when the dimensions of the system become much smaller than the electron mean free path, electrons propagate through the system ballistically. Then, conductance is not a continuous function and cannot be tracked using Ohm's law, so a different approach needs to be considered.

In Landauer's treatment, the nanojunction is imagined as a defect for propagation of the conduction electrons coming from the macroscopic electrodes.[40] The electron can be either reflected or transmitted. In an ideal case of 1D continuous nanowire between the electrodes, we assume perfect transmission probability $T = 1$. For simplicity, we also set temperature $T = 0$ K resulting in sharp drops in Fermi-Dirac distribution functions f at Fermi level E_F (Fig. 8a). Applied bias voltage V then opens an energy window eV, which enables the tunneling event between the occupied and unoccupied levels at the same energy. In this 1D example, Landauer's approach evaluates the conductance G to the following expression, called the conductance quantum G_0:

$$G = G_0 = \frac{2e^2}{h} = 77.4 \cdot 10^{-6}\ \mathrm{S} \qquad (2)$$

where e represents an elementary charge and h is a Plank's constant.

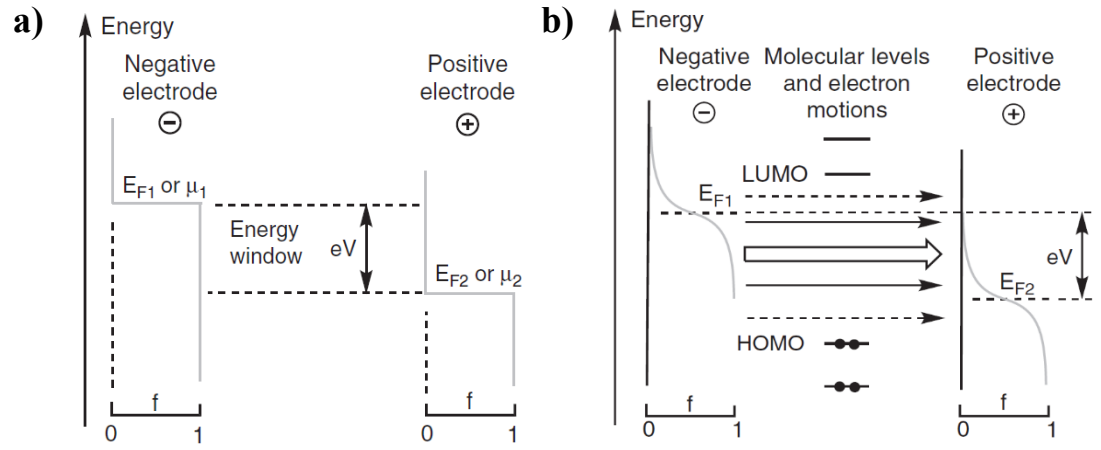

Fig. 8: a) Energy diagram for metallic electrodes connected with 1D continuous nanowire (not shown) at T = 0 K and b) Energy diagram for metal-molecule-metal junction at ambient temperature (adapted from ref. 40).

Taking into account the other two dimensions of the real junction gives rise to higher quantum states (channels). Their conductance corresponds to the multiples of the conductance quantum. When the junction is broken, the N_L and N_R channels in the left and right electrode, respectively, can couple together to form all possible pairs with different transmissions T_{ij} at Fermi energy E_F. The total conductance through the junction is then as follows:

$$G = G_0 \sum_{i=1}^{N_L} \sum_{j=1}^{N_R} T_{ij}(E_F) \tag{3}$$

When a molecule is put into the junction, the transmission is influenced by its electronic structure. High transmission values result from a molecular orbital positioned between the electrodes' Fermi levels, a state called resonance. On the contrary, low transmission is associated with off-resonant transport. As a consequence, transmission becomes a function of bias voltage. Because transmission also varies with respect to energy, integration over all energy states is needed (Eq. 4). For T > 0 K, Fermi-Dirac distributions are S-shaped functions and their difference defines the energy window (Fig. 8b). These assumptions are considered in Non equilibrium Green's function theory (NEGF), which expresses the electric current through the metal-molecule-metal junction in the following way:

$$I = \frac{2e}{h} \int_{-\infty}^{+\infty} T(E,V) \left[f\left(E - E_{F,2}\right) - f\left(E - E_{F,1}\right) \right] dE \tag{4}$$

where E represents energy, $E_{F,1}$ and $E_{F,2}$ stand for Fermi energy of the first and second electrode, respectively.

In STM-BJ experiment, conductance is measured while the tip is repeatedly pushed into the surface and pulled back. The raw data consist of thousands of breaking curves (Fig. 9). At the beginning of an individual curve (here exemplified for gold), the tip is immersed into the bulk surface electrode. Next, it is pulled away and so the junction gets narrower, and conductance decreases linearly. Gradually, a stepwise character of a conductance profile appears, which is attributed to individual quantum states. Finally, gold single-atom contact electrodes are formed, whose total conductance nearly corresponds to G_0 (Fig. 9, red ellipse). Then, a steep decrease in conductance follows, what is called a snap-back. It originates not only from the junction breaking but also from the reorganization of electrodes' adatoms back to their crystal lattices right after the junction breaks. From this point, conductance copies the exponential decay according to Eq. 1 (Fig. 9, dashed red line) until it reaches the detection limit.

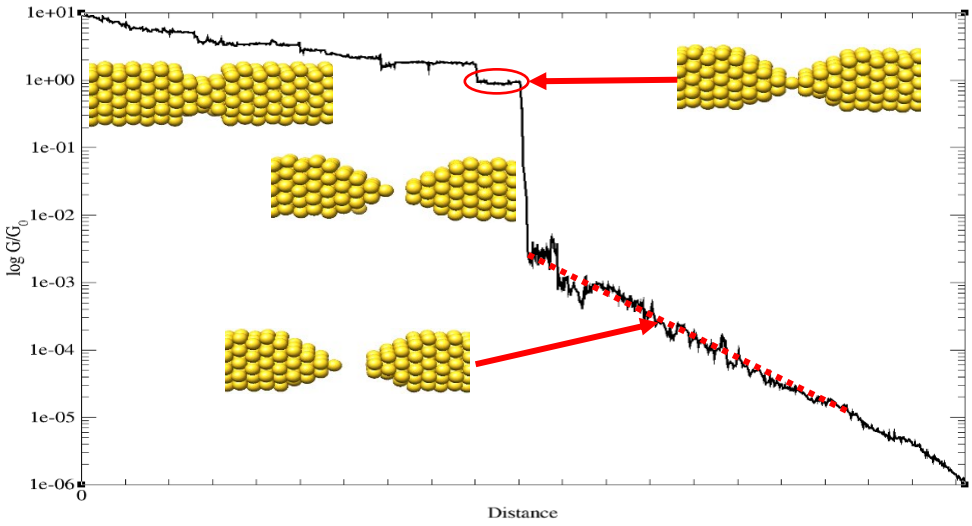

Fig. 9: An exemplary breaking curve of pure gold (adapted from ref. 41) with the depicted single-atom contact electrodes' conductance (red ellipse above) and exponential conductance decay (red dashed line below).

Since there are thousands of curves produced in one STM-BJ experiment, they are statistically processed into a form of 1D and 2D histograms (Fig. 10). While the former shows the normalized count of data points in a particular bin, the latter also represents the conductance distribution in the electrode distance. Under the sharp peak of gold point contact electrodes

at 1 G/G_0 (red line in Fig. 10), the signal of organic molecules is expected to appear in the range of approximately 10^{-1} and 10^{-5} G/G_0.

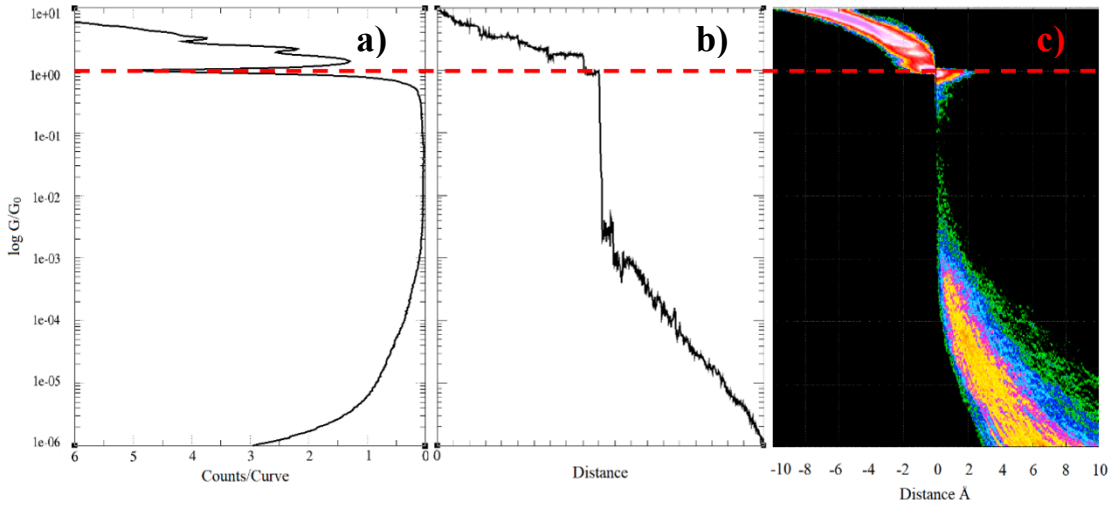

Fig. 10: Exemplary a) 1D histogram, b) a single breaking curve, and c) 2D histogram of gold with a red line showing the conductance of gold point contact electrodes, 1 G/G_0 (adapted from ref. 41).

There are two more important types of break-junction technique – mechanically controlled (MC-BJ) and electromigrated break-junction (EM-BJ).[42] The former works on similar mechanical principle like STM-BJ. However, it uses two symmetrical nanocontacts obtained from lithography technique, which are then mechanically broken and connected again repeatedly. MCBJ offers higher mechanical stability and longer junction lifetimes, which make it possible to study the vibrational modes with inelastic electron tunneling spectroscopy (IETS).[43] On the contrary, STM-BJ instrumentation is simpler and in combined STM/AFM mode, it enables measurements of the force between the two electrodes.[44]

The electromigrated break-junction also makes use of lithographically fabricated nanowire but in this case, it is broken by passing a large electric current.[45] This method is more advantageous for gating experiments since the junction can be prepared directly on the gate electrode. In contrast, the statistical evaluation is much harder as each experiment requires a new junction to be made. Also, electromigrated break-junctions made of gold suffer from migration of gold atoms at temperatures higher than 200 K.[42]

1.5 Anchoring groups

The anchoring group represents a linker element which connects the molecular bridge to the electrodes (Fig. 11). Typically, there is one anchor at either end of the molecule, but more anchors are also possible.[46] Basically, it should provide a well-defined and reproducible binding geometry, strong anchoring to the electrode, and relatively high conductance.[47]

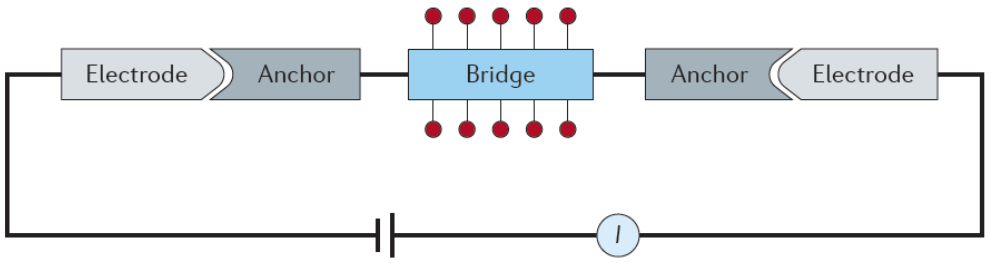

Fig. 11: Scheme of the molecular junction (adapted from ref. 48).

The anchors bind to the electrode either by donor-acceptor (dative) or covalent bond. In the dative coupling, the electrons of π- or σ-donors are shared with Lewis acidic metal atoms on the surface. Fullerenes and other π-conjugated hydrocarbons are examples of π-donors, whereas amines, thioethers, and phosphines with their lone pairs serve as σ-donors. The amines, for example, have been shown to bind selectively to the undercoordinated gold adatoms, what leads to well-defined binding geometry and gives narrower conductance distribution.[49]

The covalent bond is formed when the anchoring group chemically reacts with the metal surface. Since the experiments are usually done on a gold surface, the most widely used anchoring group is thiol[47] thanks to high affinity of sulfur to gold. The covalent linkages are advantageous as they couple strongly to the electrodes. As such, Au-S bond is much more thermodynamically stable than dative bond made by amine group.[50] Anyway, thiols suffer from polymerization through oxidation to give polydisulfides.[51] It is difficult then to ensure that conductance of a monomer is measured. This is no longer an issue when thiol group is protected, for example, with acetyl residue. Acetyl-protected thiols can lose their acetyl group on a gold surface and bind to it covalently. This binding was observed even without addition of any external base, though higher thiol concentration was required.[51]

The anchoring group also influences the character of charge transport through the junction. Depending on the electron donating (-NH_2, -SR, -PR_3) or

withdrawing (-CN, -NO_2, -F) nature of the anchor, it either raises or lowers the molecular orbital energy levels. Then, HOMO (Highest Occupied Molecular Orbital) or LUMO (Lowest Unoccupied Molecular Orbital) gets closest to the Fermi energy level of the electrodes (E_F) and dominates the transport. Electrons or holes then mediate the current for HOMO- or LUMO-dominated conductance. The character of charge transport can be determined theoretically[52] or from thermopower measurements.[53]

1.6 Metals

The most widely used electrode material is gold because of its plasticity and chemical inertness, which makes it easy to work with even at ambient conditions.[48] Other possible metals that have been used are silver,[54] platinum,[55] or palladium[56] but these may require more sophisticated instrumentation like air-free or ultra-high vacuum conditions.[48]

Since silver's electronic structure is not much different from that of gold, similar experiments were carried out on silver surfaces. Conductance of a series of alkanes **C3**–**C6** (3–6 CH_2 groups) and oligophenyls **P1**–**P3** (1–3 aromatic rings) terminated with amino groups (both shown in Fig. 12c) were determined on both silver and gold (Fig. 12a,b).[57] In all cases, silver junctions provided lower conductance values and broader conductance distributions. The authors attribute this to higher Fermi energy of silver (–4.7 eV) than gold (–5.3 eV). Therefore, E_F is further from HOMO, which dominates the transport through these compounds, and so the conductance is lower.

Another feature that strongly influences conductance of a junction is the density of states (DOS) of a metal near Fermi level.[36] Therefore, high values of DOS of platinum and palladium motivate their use in building metal-molecule junctions. The effect of these metals on conductance was demonstrated on a series of alkyldiisothiocyanates, where two to three times higher conductance was found for platinum and palladium junctions when compared to gold ones.[56]

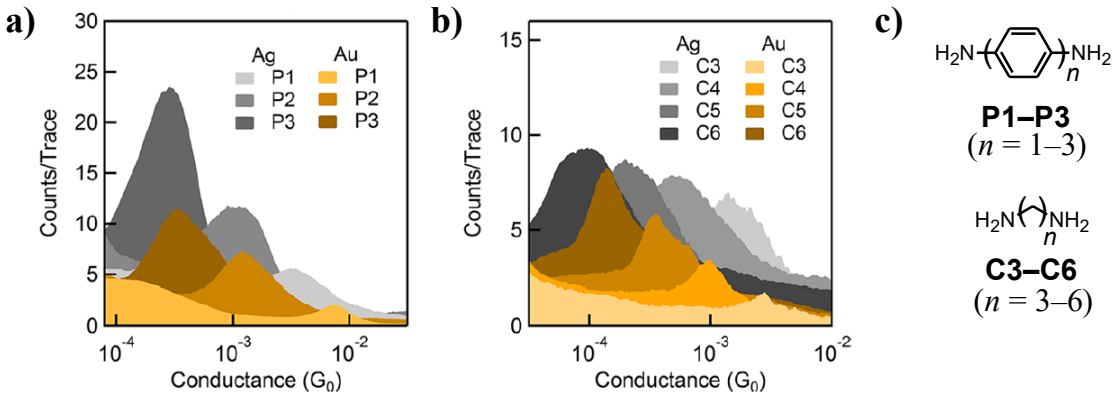

Fig. 12: Logarithmic conductance histograms of oligophenyls **P1**–**P3** a) and oligoalkanes **C3**–**C6**, b) on both Au and Ag, and c) structures of oligophenyls **P1**–**P3** and oligoalkanes **C3**–**C6** terminated with amino groups (adapted from ref. 57).

1.7 Chirality-induced spin selectivity

In 1999, Naaman and co-workers firstly observed spin-dependent photoelectron transmission through a thin film of chiral molecules deposited on a gold substrate.[58] There was no explanation for their observation at the time, but several theoretical papers have been published since then.[59] Anyway, this effect, termed chirality-induced spin selectivity (CISS), is not fully understood even two decades later.[60]

A simplified model was later published by Naaman, Paltiel, and Waldeck.[61] In this model, an electron propagates through a chiral molecule, for example helicene, along its helical backbone (Fig. 13) and experiences electrostatic forces from the other electrons and nuclei in the molecule. The moving electron is kept within the helical path by a centripetal force $\overrightarrow{F_c}$, which is a radial component of the total electrostatic force $\overrightarrow{E_r}$ acting on the electron. In the rest frame of the moving electron, the centripetal force $\overrightarrow{F_c}$ is equivalent to a Lorentz force produced by an effective magnetic field $\overrightarrow{B_{\text{eff}}}$ parallel to the axis of propagation z. According to the Zeeman effect, the two spin states of the electron in the magnetic field give rise to two different energy states, *i.e.*, two different energy barrier heights. As the transmission depends exponentially on the barrier height, the two spin states are passed through the molecule with different probability, what results in a spin selective electron transport.

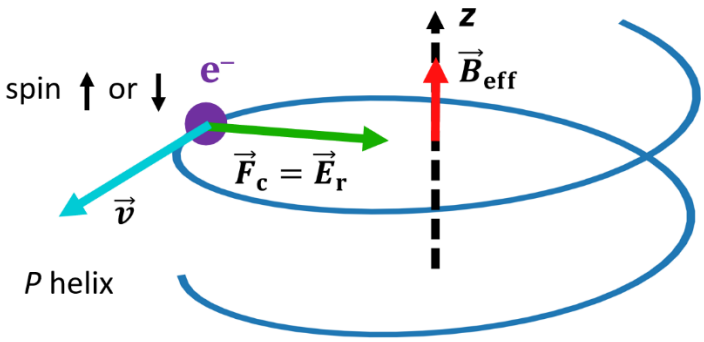

Fig. 13: Scheme of an electron passing through a helical molecule.

The CISS effect represents a new link between electron spin and chirality of molecules. It has been observed on various chiral systems such as DNA,[62] oligopeptides,[63] chiral organic polymers,[64] and cationic helicenes.[11]

In photoelectron experiments with DNA, Naaman and co-workers[62] measured spin polarization (*SP*) up to approximately 60 % for dsDNA fragment of 78 bp deposited on a gold surface. This value corresponds to a ratio of spin up or down electron count $I_{\uparrow}$:$I_{\downarrow}$ of 4:1 as *SP* is expressed as follows:

$$SP = \frac{I_{\uparrow} - I_{\downarrow}}{I_{\uparrow} + I_{\downarrow}} \tag{5}$$

In a similar type of experiment, Ernst and co-workers studied photoemitted electrons from a monolayer of [7]helicene on Cu(332), Ag(110) and Au(111) surfaces.[60] They also found that the electrons were spin-polarized and *SP* on these metals was 11.7, 15.9 and 15.7 %.

Beside photoemission experiments, magnetic conductive probe atomic force microscopy (mCP-AFM) was used by Naaman and co-workers to study spin polarization (Fig. 14a).[11] In two setups, they examined the conductance of cationic [4]helicene **13** (Fig. 14b) in two opposite magnetic field orientations. On a ferromagnetic nickel substrate, helicene films did not form any oriented structure and then, when scanned with a nonmagnetic tip, they showed only little *SP* of approx. 4 % (here *SP* is defined similarly to Eq. 5 only with $I_{\uparrow}$, $I_{\downarrow}$ representing spin up or down electric current). In the other case, an organized helicene monolayer was observed on highly oriented pyrolytic graphite (HOPG) and with magnetized Fe-coated Si tip, the authors measured *SP* = 49 or 45 % for *P* and *M* enantiomer. All these

results point at a new possible application of organic compounds, including helicenes, to construct spin-filtering devices based on CISS effect.

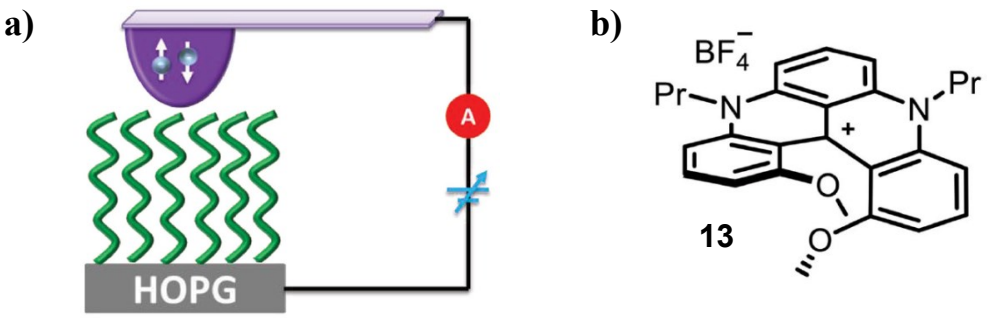

Fig. 14: a) Scheme of mCP-AFM experiment with a magnetic tip on HOPG and b) structure of cationic helicene **13** (adapted from ref. 11).

2 Goals

The ultimate goal of this *thesis* is to examine the single-molecule conductance of helicenes, particularly to determine, how the conductance changes for helicenes of different length.

The first objective is to prepare two representative acetylsulfanyl helicenes **14** and **15** (Fig. 15) with 5 and 9 *ortho*-annulated aromatic rings in its main skeleton. [9]Helicene **15** will be then resolved into enantiomers and a model compound biphenyl **16** of similar length to [5]helicene **14** will be synthesized.

The second objective is to obtain single-molecule conductance of these compounds using scanning tunneling microscopy-based break-junction technique.

Finally, the results are planned to be compared with theoretical calculations and data from X-ray diffraction experiments.

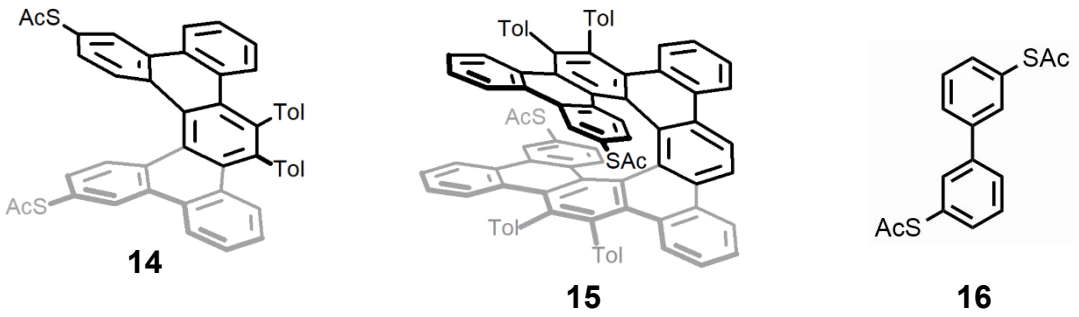

Fig. 15: Target acetylsulfanyl [*n*]helicenes **14** and **15** for *n* = 5 and 9, and a model compound **16**.

3 Results and discussion

3.1 Organic synthesis

The following synthesis of acetylsulfanyl [*n*]helicenes **14** and **15** (*n* = 5 or 9) was designed based on previous research in Ivo Starý Group.[30] The odd numbers of central aromatic rings come from symmetry of oligoalkyne precursor, which is prepared by consecutive Sonogashira and Suzuki coupling reactions and finally transformed to corresponding helicene in [2+2+2] oligoalkyne cyclotrimerization (Scheme 4). Acetylsulfanyl anchoring groups are installed by substitution of chlorine atoms attached during the synthesis. The tolyl groups are incorporated to increase the solubility the of the target helicenes.

Scheme 4

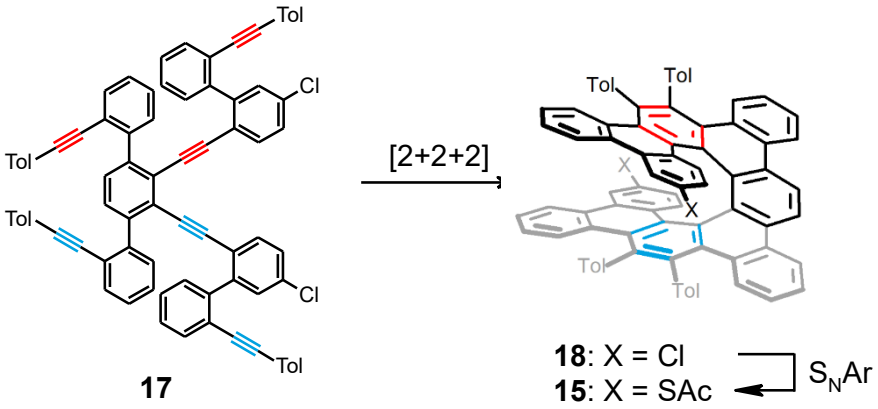

3.1.1 Synthesis of [5]helicene 14

A commercially available halide **19** was chosen as a starting material for synthesis of [5]helicene **14** because it is possible to make it react successively at iodine and bromine atom in coupling reactions while the chlorine atom remains intact. In the first step, the halogen derivative **19** was transformed into halogenated alkyne **20** by means of a double Sonogashira coupling reaction with gaseous acetylene (Scheme 5) according to the literature.[65] The reaction was stirred in acetylene atmosphere at 55 °C for 20 h to afford alkyne **20** (86 % yield), which was then subjected to Suzuki coupling reaction with boronic acid **22**. Heating in mixture of toluene:*n*-PrOH:H_2O (4:4:1) at 90 °C for 3 h led to triyne **21** in 75 % yield.

Scheme 5

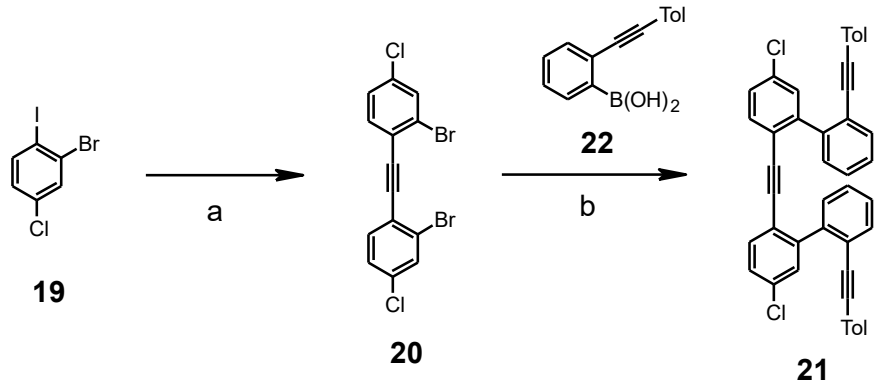

a) acetylene atmosphere, $Pd(PPh_3)_4$ (10 mol%), CuI (20 mol%), DIPA, 55 °C, 20 h, 86 %
b) **22** (3.0 eq.), $Pd(PPh_3)_2Cl_2$ (10 mol%), K_2CO_3 (3.0 eq.), toluene:*n*-PrOH:H_2O (4:4:1), 90 °C, 3 h, 75 %

Synthesis of boronic acid **22** started from 2-bromo-1-iodobenzene **23** by a consecutive Sonogashira coupling-TIPS deprotection-Sonogashira coupling reaction sequence in one pot (96 % yield, Scheme 6). Alkyne **24** was then lithiated with *n*-BuLi and after addition of triisopropylborate, it yielded boronic acid **22** in 94 %.

Scheme 6

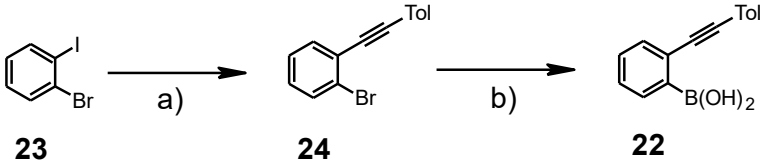

a) 1) TIPSA (1.05 eq.), $Pd(PPh_3)_2Cl_2$ (1 mol%), CuI (2 mol%), DIPA, 0 °C, overnight
2) *n*-TBAF (2.5M, 1.5 eq.), RT, 30 min
3) 4-iodotoluene (3.0 eq.), $Pd(PPh_3)_2Cl_2$ (1 mol%), CuI (2 mol%), DIPA:toluene (1:1), from 0 °C to RT, 12 h, 96 %, (over 3 steps)
b) 1) *n*-BuLi (1.6M, 1.3 eq.), THF, –78 °C, 45 min
2) B(O*i*-Pr)$_3$ (1.5 eq.), from –78 °C to RT, 30 min
3) HCl (1M), RT, 1 h, 94 % (over 3 steps)

Triyne **21** was further transformed into dichloro[5]helicene **25** by Ni-complex mediated [2+2+2] cyclotrimerization by heating in toluene to 140 °C in a pressure flask for 1.5 h (Scheme 7). Finally, target [5]helicene **14** was obtained *via* nucleophilic aromatic substitution in NMP at 200 °C. Methyl thiolate was generated *in situ* from dimethyl disulfide by reduction with sodium and the reaction mixture was quenched with acetyl chloride to give final bis(acetylsulfanyl)-[5]helicene **14** in 89 % yield.

Scheme 7

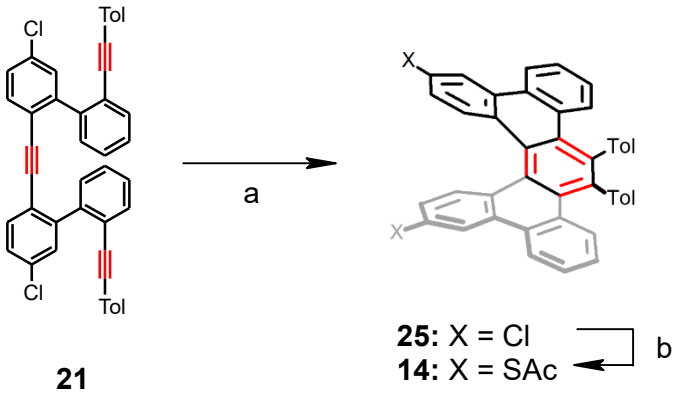

a) $Ni(PPh_3)_2(CO)_2$ (60 mol%), toluene, 140 °C, 1.5 h, 45 %
b) 1) Na (45.0 eq.), DMDS (35.0 eq.), NMP, 200 °C, 3 h
2) AcCl (62.0 eq.), from 0 °C to RT, 2 h, 89 % (over 2 steps)

3.1.2 Synthesis of [9]helicene 15

The starting synthetic block, tetrayne **26**, was previously prepared in our group by an internship student Martin McLaughlin (University of Bristol, UK). At the beginning, tetrayne **26** was coupled with organic halide **19** *via* double Sonogashira coupling reaction in mixture DIPA:toluene at room temperature to give dibromide **27** in 86 % yield (Scheme 8). After that, the double Suzuki coupling of dibromide **27** with boronic acid **22** was carried out in mixture toluene:*n*-PrOH:H_2O (4:4:1) at 90 °C and afforded the doubly tolylated hexayne **28** (80 %, Scheme 9).

Scheme 8

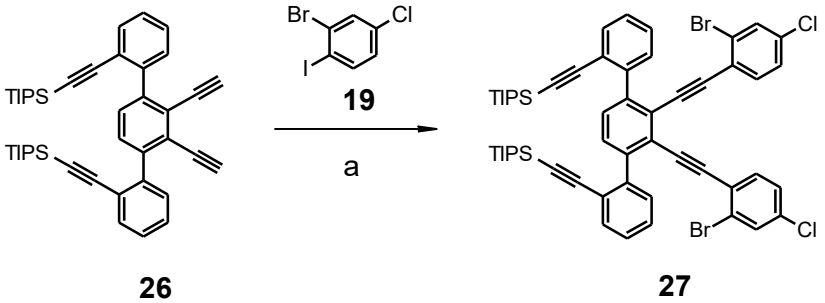

a) **19** (3.0 eq.), $Pd(PPh_3)_2Cl_2$ (5 mol%), CuI (10 mol%), DIPA:toluene (4:1), RT, overnight, 86 %

Scheme 9

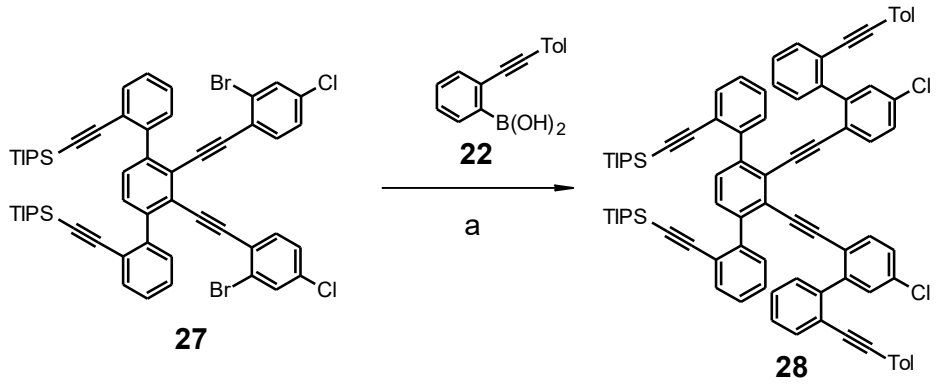

a) **22** (3.0 eq.), $Pd(PPh_3)_2Cl_2$ (8 mol%), K_2CO_3 (3.0 eq.), toluene:*n*-PrOH:H_2O (4:4:1), 90 °C, 3 h, 80 %

In the next step, two TIPS protecting groups of hexayne **28** were cleaved off by an addition of tetra-*n*-butylammonium fluoride trihydrate (Scheme 10) followed by another Sonogashira coupling reaction in one pot. In this way, two TIPS groups were exchanged for two tolyl groups leading to quadruply tolylated hexayne **17** in 78 % yield. Double [2+2+2] cyclotrimerization mediated by Ni-complex in toluene at 140 °C provided dichloro[9]helicene **18** (41 % yield).

Scheme 10

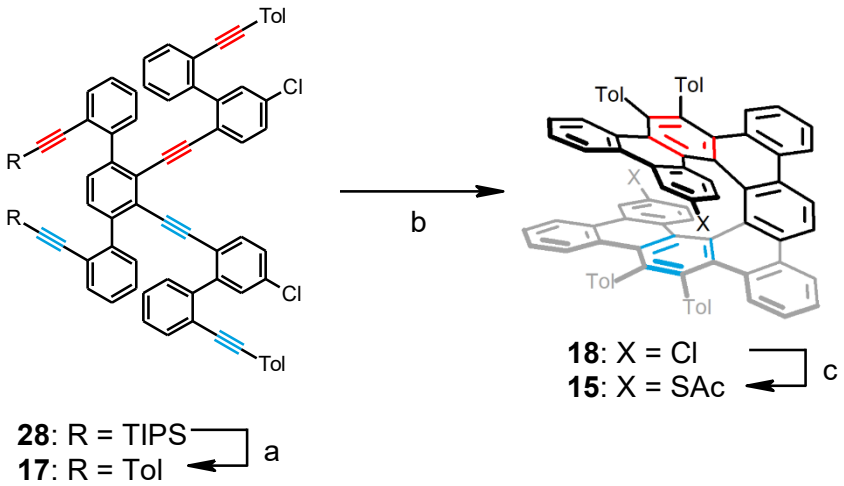

a) 1) *n*-TBAF (1M, 3.0 eq.), toluene, RT, 20 min
2) $Pd(PPh_3)_2Cl_2$ (5 mol%), CuI (10 mol%), 4-iodotoluene (2.4 eq.), DIPA:toluene (1:2), RT, 20 h, 78 % (over 2 steps)
b) $Ni(PPh_3)_2(CO)_2$ (60 mol%), toluene, 140 °C, 1.5 h, 41 %
c) 1) Na (50.0 eq.), DMDS (31.0 eq.), NMP, 200 °C, 5 h
2) AcCl (70.0 eq.), from 0 °C to RT, 1 h, 58 % (over 2 steps)

In the end, the chlorine atoms were exchanged for acetylsulfanyl groups by nucleophilic aromatic substitution to give [9]helicene **15** in 58 % (Scheme 10). When compared with [5]helicene **14**, the yield was approx. one third lower (58 % vs. 89 %) and the decrease was attributed to the larger sterical hindrance around the sites where substitution took place on the longer [9]helicene **15**.

3.1.3 Synthesis of biphenyl 16

Bis(acetylsulfanyl)biphenyl **16** was designed as a model congener of [5]helicene **14** according to the following simplification (Fig. 16). The molecular structure of helicene **14**, though distorted, resembles benzo[*ghi*]perylene **29**, which can be graphically reduced to biphenyl **16**.

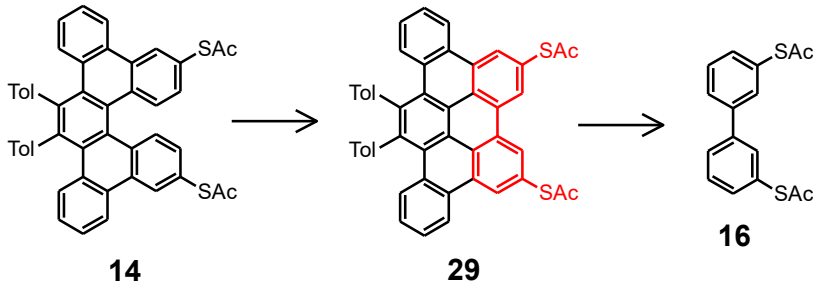

Fig. 16: The structural relevance of [5]helicene **14** to benzo[*ghi*]perylene **29** and biphenyl **16** (colored red in a structure of perylene **29**).

To provide biphenyl **31**, Ullmann coupling reaction of two equivalents of halide **30** was carried out at first. Activated copper powder was used as a catalyst, but the reaction did not yield the desired product. The Suzuki coupling reaction between halide **30** and boronic acid **32** was chosen as an alternative and afforded biphenyl **31** in 59 % yield (Scheme 11). Then, nucleophilic aromatic substitution was utilized to give biphenyl **16** (79 %).

Scheme 11

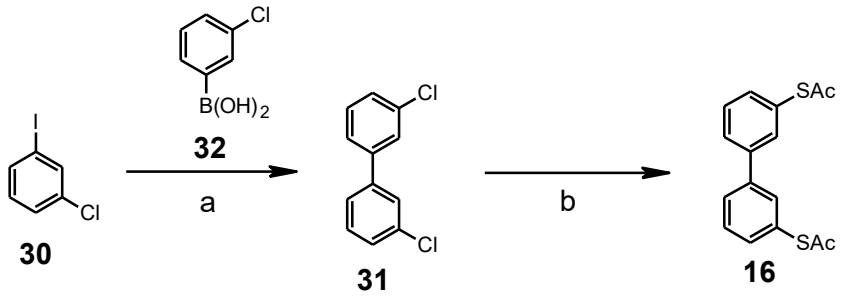

a) **32** (1.5 eq.), $Pd(PPh_3)_2Cl_2$ (8 mol%), K_2CO_3 (3.0 eq.), toluene:*n*-PrOH:H_2O (20:20:1), 90 °C, 3 h, 59 %
b) 1) Na (50.0 eq.), DMDS (31.0 eq.), NMP, 200°C, 4 h
2) AcCl (70.0 eq.), from 0 °C to RT, 1 h, 79 % (over 2 steps)

3.2 Separation of target [9]helicene 15 into enantiomers

Since racemization barrier of [5]helicenes is not high enough to avoid racemization in solution at room temperature,[12] only the target [9]helicene **15** was resolved. The separated enantiomers of racemic [9]helicene **15** might be used in future in STM-BJ experiments in magnetic field to measure the CISS effect. The resolution was carried out using semi-preparative chiral HPLC column Amylose SA. Enantiomeric excess was determined on analogous analytical column ($t_{R,+}$ = 7.8 min, $t_{L,-}$ = 11.2 min, heptane:IPA 98:2) and chromatograms from these measurements are shown in Fig. 17. For more details see the *Experimental section*.

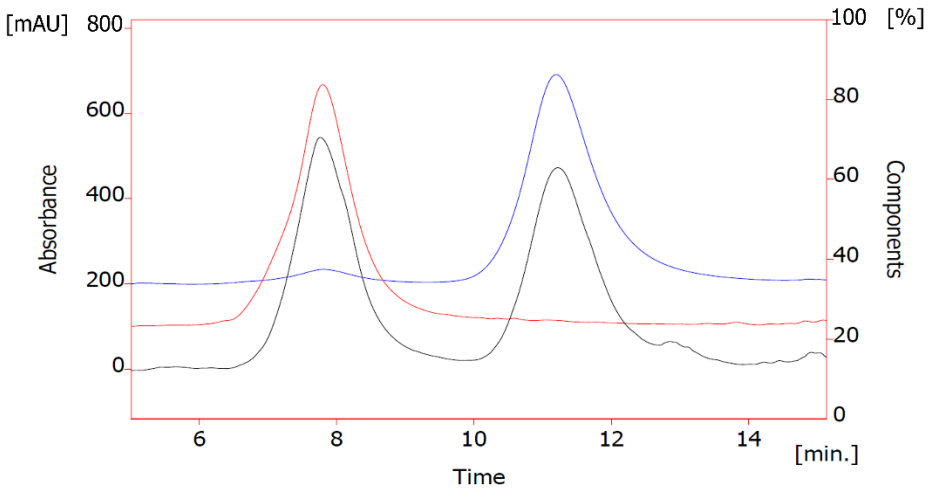

Fig. 17: HPLC chromatogram of *rac*-**15** (black), (+)-(*P*)-**15** (red,98 % *ee*), (–)-(*M*)-**15** (blue, 90 % *ee*). Individual chromatograms are offset in y axis for clarity.

3.3 Solubility comparison of [5]helicenes 14 and 33

Tolyl groups were initially incorporated into the molecule of [5]helicene **14** to increase its solubility. To prove this effect, similar [5]helicene **33**, which differs only in the absence of tolyl groups, was chosen for a brief solubility study. The organic solvents, such as DCM, acetone, and toluene, were used and the tolylated helicene **14** was found to be roughly 4 times more soluble in DCM than the non-tolylated helicene **33** (Fig. 18). The solubility of helicene **14** was even 50 times higher than helicene **33** in acetone or toluene. For the solubility data see the *Experimental section*.

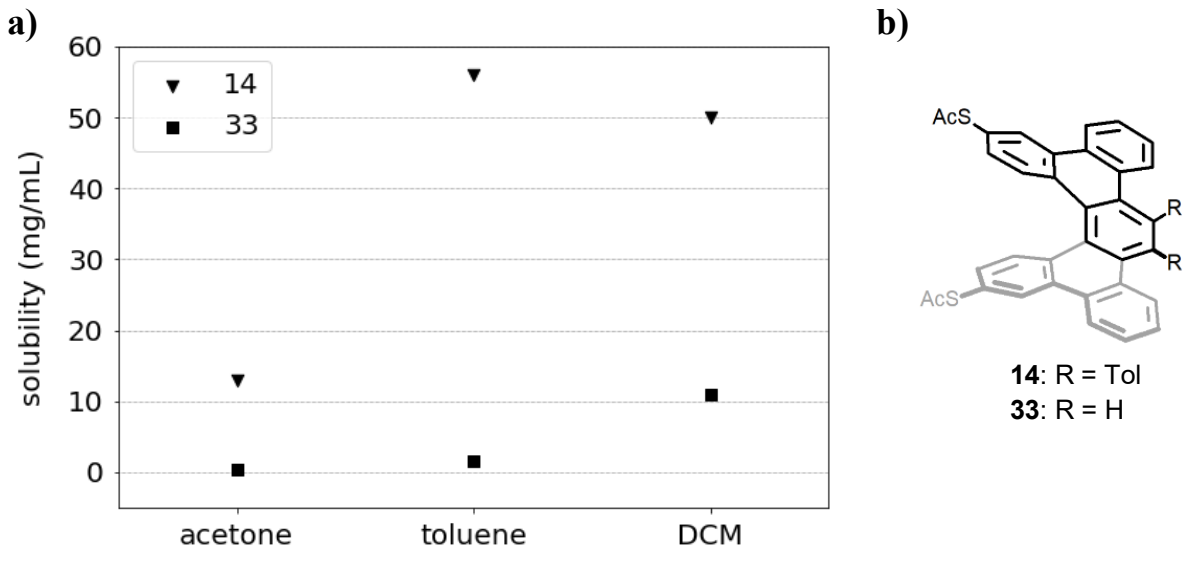

Fig. 18: a) Solubility of the tolylated helicene **14** compared to the non-tolylated helicene **33** in acetone, toluene, and DCM and b) structures of [5]helicenes **14** and **33**.

3.4 STM-BJ measurements

To prove the reliability and reproducibility of the molecular conductance measurements, two simple compounds, stilbene **34**[66] and biphenyl **16**, have been chosen for the first experiments (Fig. 19). As already mentioned, biphenyl **16** is a simplified congener of [5]helicene **14** and their sulfur-sulfur distances obtained from DFT calculations in Gaussian09[67] are almost the same (9.27 Å for **16** vs. 9.31 Å for **14**). Similarly, the sulfur-sulfur distance on

stilbene **34** (13.15 Å) is very close to that of [9]helicene **15** (13.37 Å) according to DFT calculations.

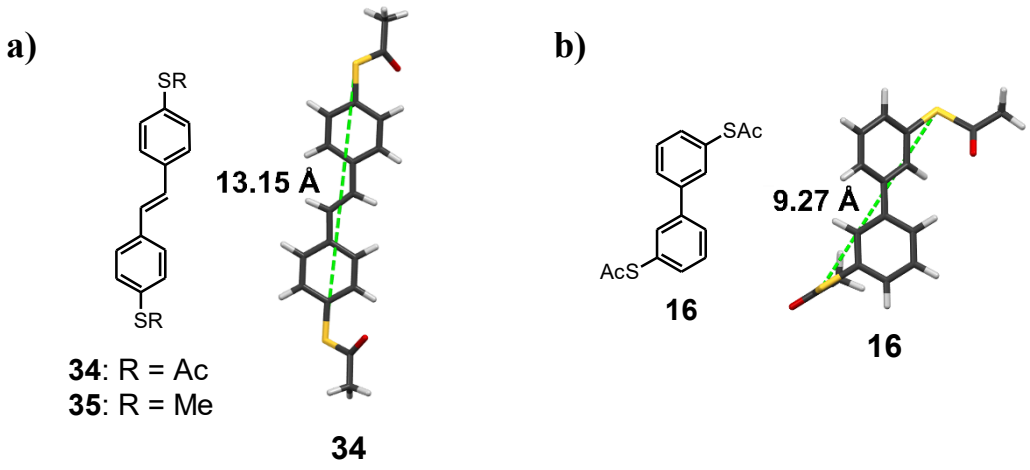

Fig. 19: a) Structures of stilbenes **34** and **35**, and the DFT optimized structure of stilbene **34** with the depicted sulfur-sulfur distance and b) analogous structures of biphenyl **16** with the depicted sulfur-sulfur distance from DFT calculation.

3.4.1 Stilbene 34

In the first measurement, conductance of stilbene **34** was determined to have maximum at $4 \cdot 10^{-3}$ G/G_0, which is in a full agreement with data obtained previously in our group. A very similar molecule **35** differing only in the anchoring groups (Me instead of Ac) was studied by Venkataraman.[68] The conductance of stilbenes **34** and **35** appears close to each other as is shown in logarithmic 1D histogram (Fig. 20).

A 2D histogram (Fig. 21) then shows a correlation of the conductance values to the electrode displacement. The conductance plateau of stilbene **34** ends at a lower effective length of molecule (~9 Å, white bar in Fig. 21) than expected when compared to the sulfur-sulfur distance from DFT calculations (13.15 Å). This may come from a snap-back relaxation of electrodes,[69] which leads to widening the actual electrode displacement relatively to the instrumental displacement.

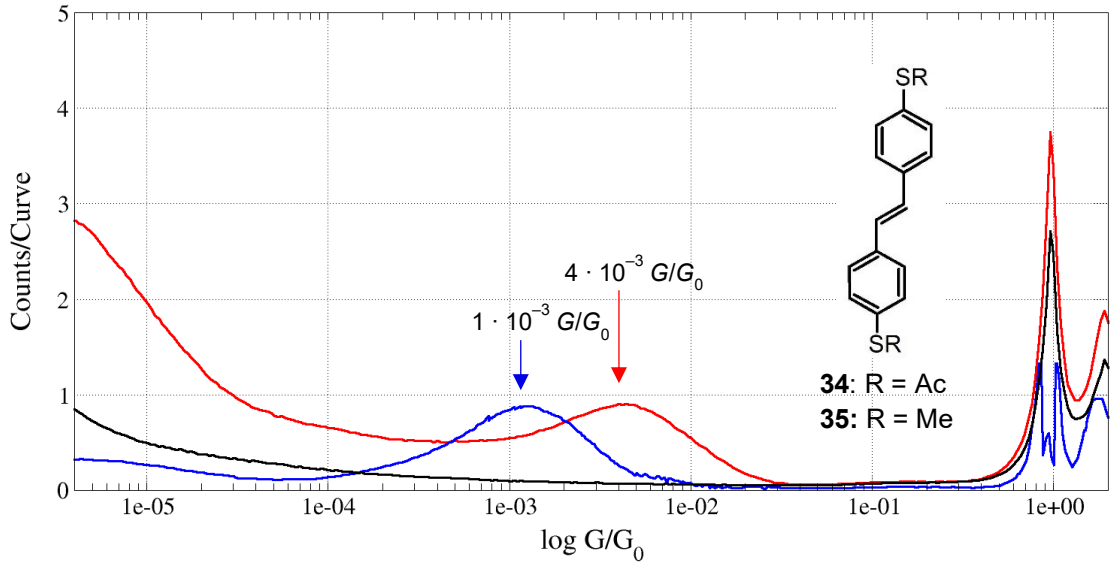

Fig. 20: Logarithmic conductance histogram of stilbenes **34** (red), **35**[68] (blue) and blank gold sample (black) with the denoted experimental conductance values.

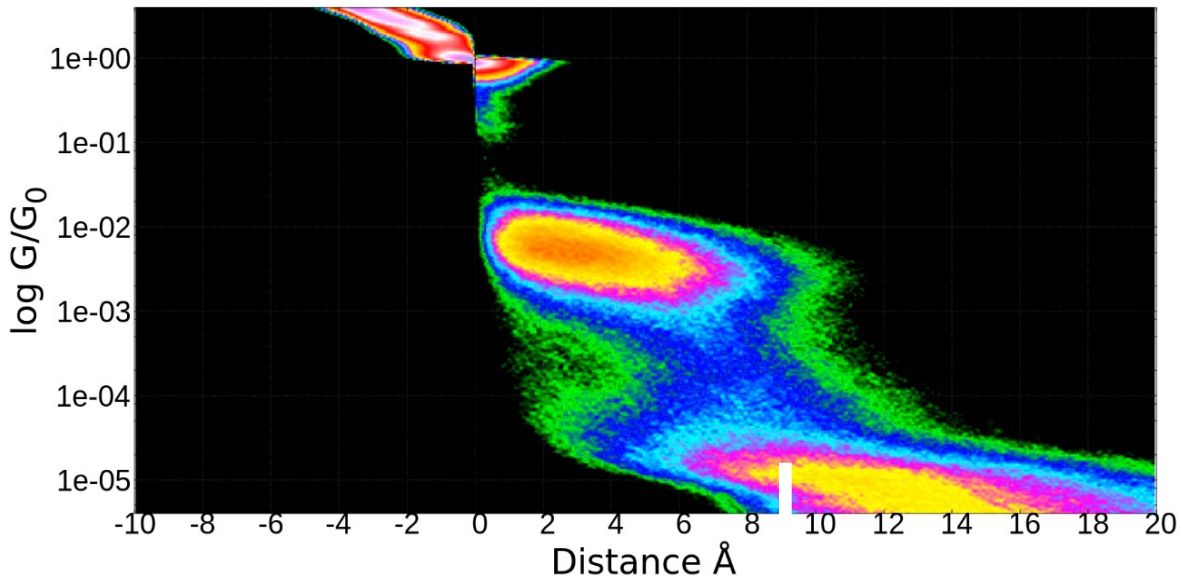

Fig. 21: 2D conductance-distance histogram of stilbene **34**.

3.4.2 Biphenyl 16

The STM-BJ measurement of biphenyl **16** showed a low conductance with peak maximum at $1 \cdot 10^{-4}$ G/G_0 (Fig. 22). It can be attributed to *meta*-linked character of this molecule, which typically results in low, or no conductance caused by negative quantum interference.[48]

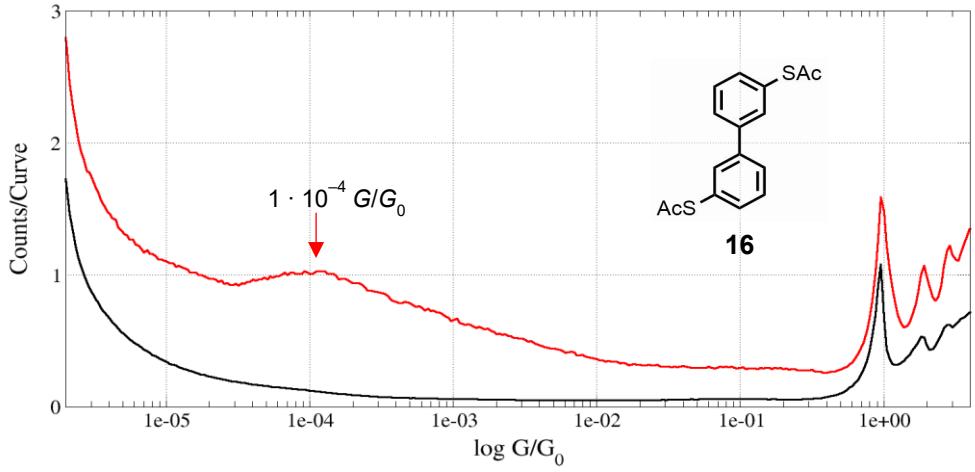

Fig. 22: Logarithmic conductance histogram of biphenyl **16** (red) and blank gold sample (black) with the denoted experimental conductance value.

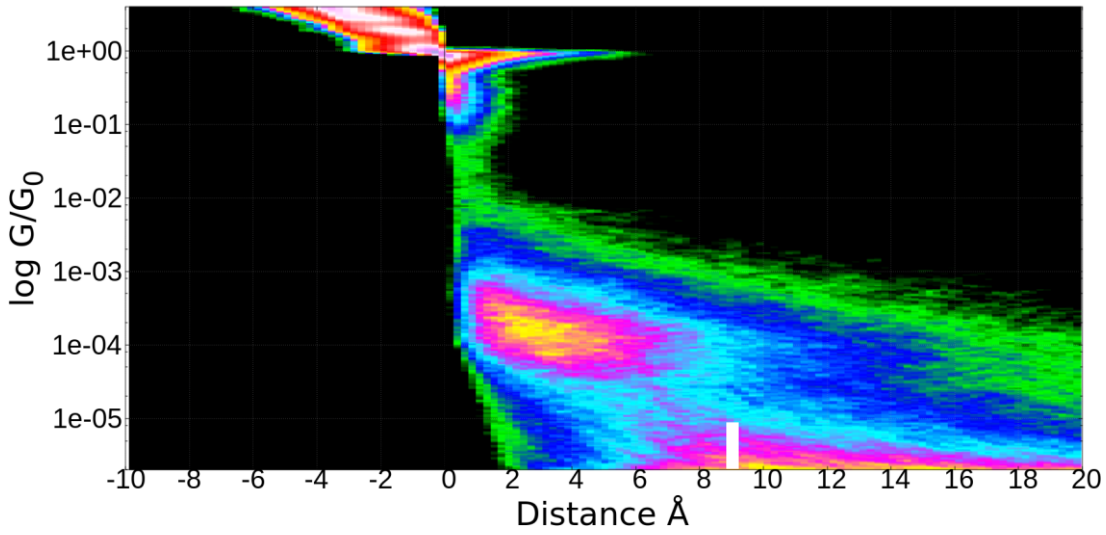

Fig. 23: 2D conductance-distance histogram of biphenyl **16**.

In a corresponding 2D histogram (Fig. 23) we can see the distribution of conductance in electrode-electrode distance. The end of conductance plateau indicates the effective molecular length of ~ 9 Å (white bar in Fig. 23), which is in an agreement with distance between the sulfur atoms on biphenyl **16** (9.27 Å according to DFT calculation).

3.4.3 [5]Helicene 14

After introductory measurements, which proved the validity of the STM-BJ experimental method, the single-molecule conductance of [5]helicene **14** was studied. Several illustrative breaking curves are depicted in Fig. 24, where conductance through helicene **14** is shown between 10^{-3} and 10^{-4} G/G_0. Moreover, the bright and the dark green curve have two horizontal sections in this interval, which seem to correspond to a switching between a low and high conductance state of helicene **14**. This phenomenon most likely comes from the ability of acetylsulfanyl groups to bind to the gold electrode both by oxygen or sulfur atom.

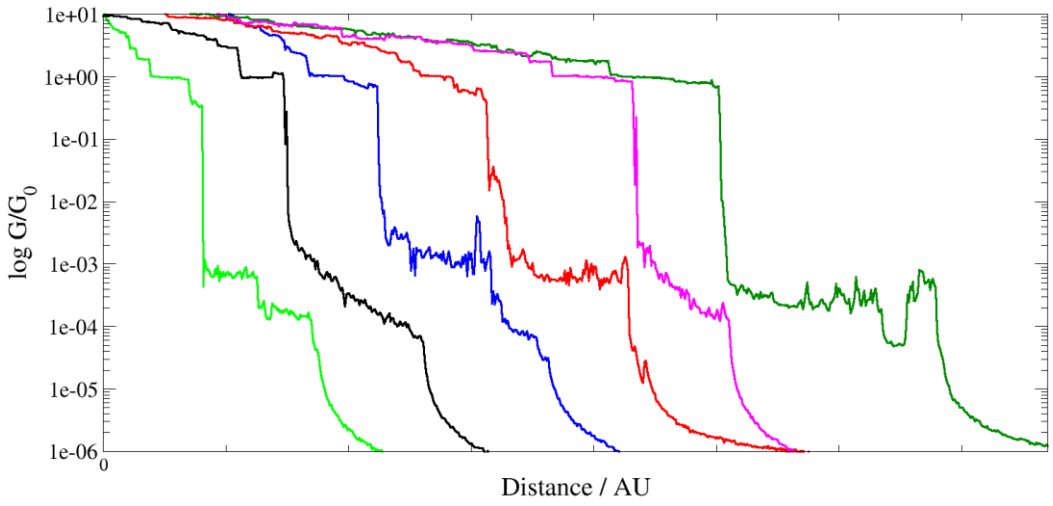

Fig. 24: Exemplary breaking curves from STM-BJ experiment of [5]helicene **14**.

The actual selected breaking curves afforded two conductance peaks (red curve in Fig. 25), when processed into a logarithmic histogram (Fig. 25). The high conductance peak (maximum at $1 \cdot 10^{-3}$ G/G_0) represents the sulfur-bound state and the low conductance peak (maximum at $8 \cdot 10^{-5}$ G/G_0) stands for the oxygen-bound state. Similar behavior has been already observed in our group for [5]helicene **33** (inset and blue curve in Fig. 25), which unlike [5]helicene **14** bears no tolyl groups. Above that, these two bonding states of the acetylsulfanyl

group were observed previously by Jelínek in a collaboration with our group in UHV STM.[70] The authors could even switch between these states on [7]helicene **36** (Fig.27a) by mechanical contact with STM tip or by application of bias voltage.

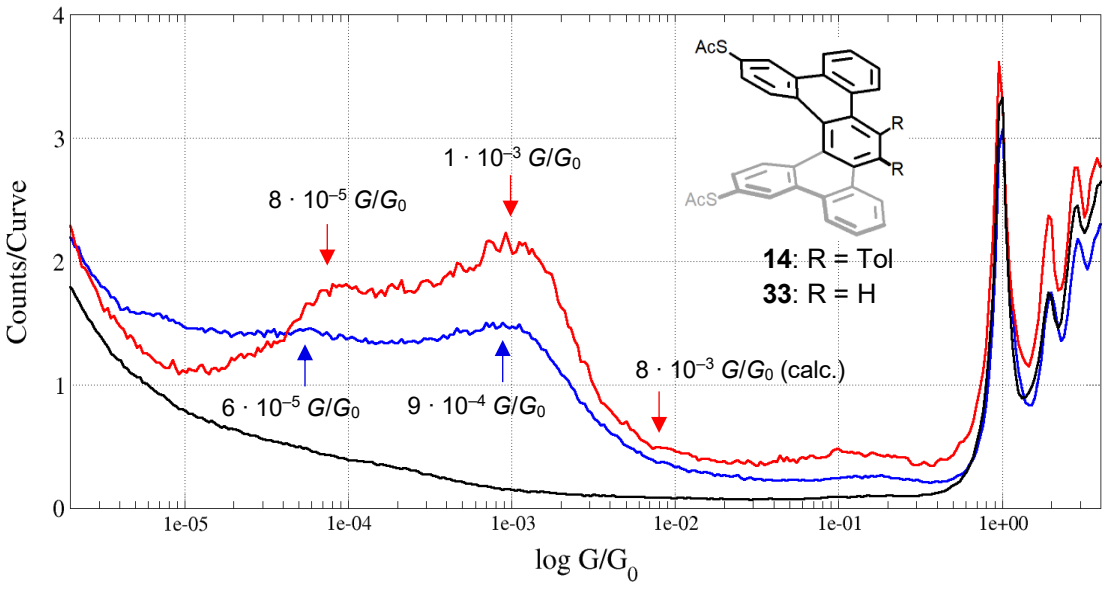

Fig. 25: Logarithmic conductance histogram of [5]helicenes **14** (red, inset structures) and **33** (blue) and blank gold sample (black) with the denoted experimental and calculated conductance values.

Two different states were also observed in the 2D conductance histogram (Fig. 26). The high conductance plateau ends at ~8 Å (left white bar in Fig. 26), what is of slightly lower value than the sulfur-sulfur distance on helicene **14** obtained from DFT calculations (9.31 Å). On the contrary, the plateau length matches very well with the S-S distance disclosed by X-ray diffraction measurement (8.21 Å, Fig. 27b).

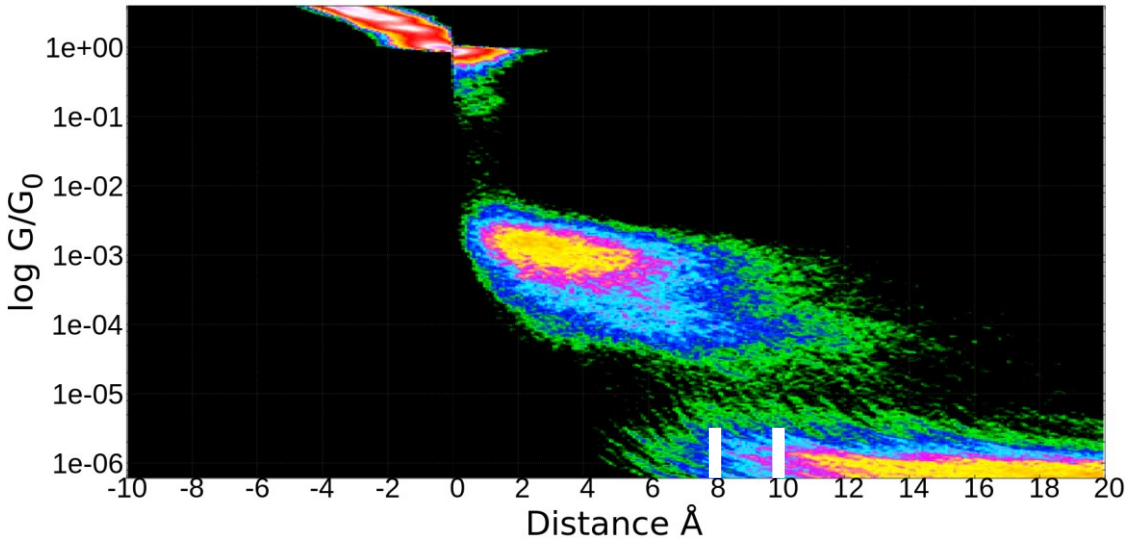

Fig. 26: 2D conductance-distance histogram of [5]helicene **14**.

The second low conductance plateau is ascribed to the oxygen-bound state and is of ~2 Å shifted to longer electrode separation (right white bar in Fig. 26). The same observation was made by Starý and Jelínek,[70] who found a length difference of 1.8 Å between analogous two states on [7]helicene **36** (Fig. 27a) in UHV STM. Beside that, plateaus of both states end at similar distance like the model biphenyl **16** (~9 Å).

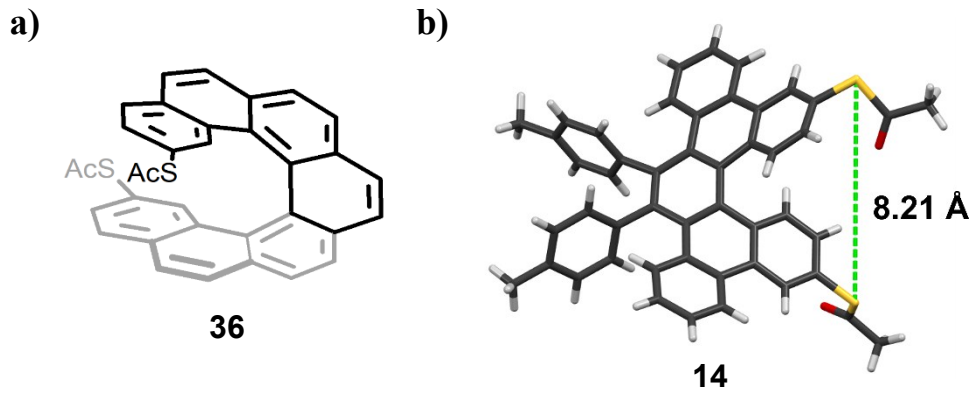

Fig. 27: a) Structure of [7]helicene **36** and b) X-ray structure of helicene **14** with the depicted sulfur-sulfur distance.

The experimental conductance of the sulfur-bound state was also compared with theoretical calculations. After optimization of molecular geometry with DFT/B3LYP in Gaussian09, the molecule of [5]helicene **14** was placed between Au(111) electrodes in QuantumWise ATK (Fig 28).[71,72,73] Setting the Au-S distance to 2.66 Å according to

literature,[74] the slightly higher conductance of $8 \cdot 10^{-3}$ G/G_0 was obtained (inset value in Fig. 25), which is in agreement in order of magnitude with the experimental value ($1 \cdot 10^{-3}$ G/G_0). Beside that, calculated transmission pathways show that the tolyl groups do not significantly participate on electron transport through helicene molecule (Fig. 29).

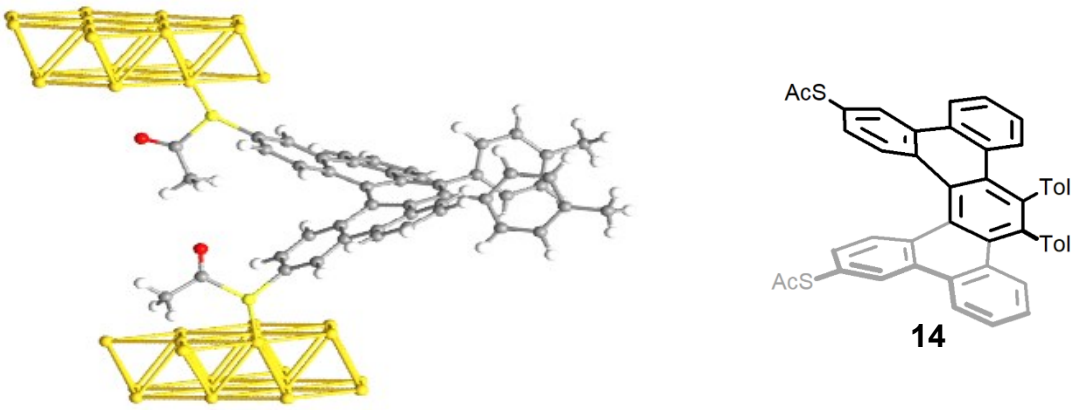

Fig. 28: Helicene **14** in a gold-helicene-gold junction (electrodes were cut for clarity).

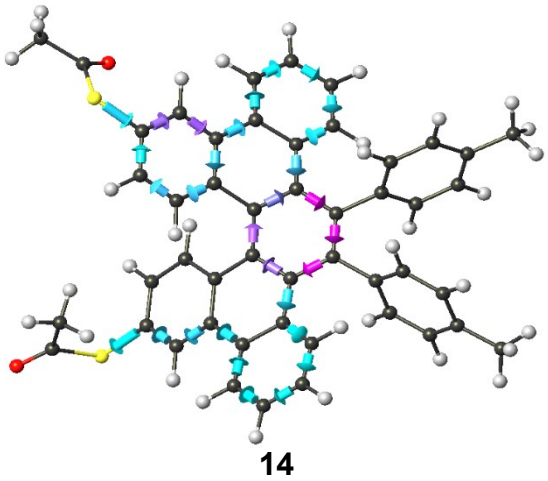

Fig. 29: Relative weight of transmission pathways represented by arrows (from blue for low to magenta for high) showing negligible electron transmission through tolyl groups of [5]helicene **14**.

3.4.4 [9]Helicene 15

Finally, the single-molecule conductance of [9]helicene **15** was measured. Unlike the rigid molecules **34** and **16**, molecular structure of long helicene **15** offers greater conformational freedom. As a result, courses of breaking curves are much more variable (Fig. 30) and no two distinguishable states were observed.

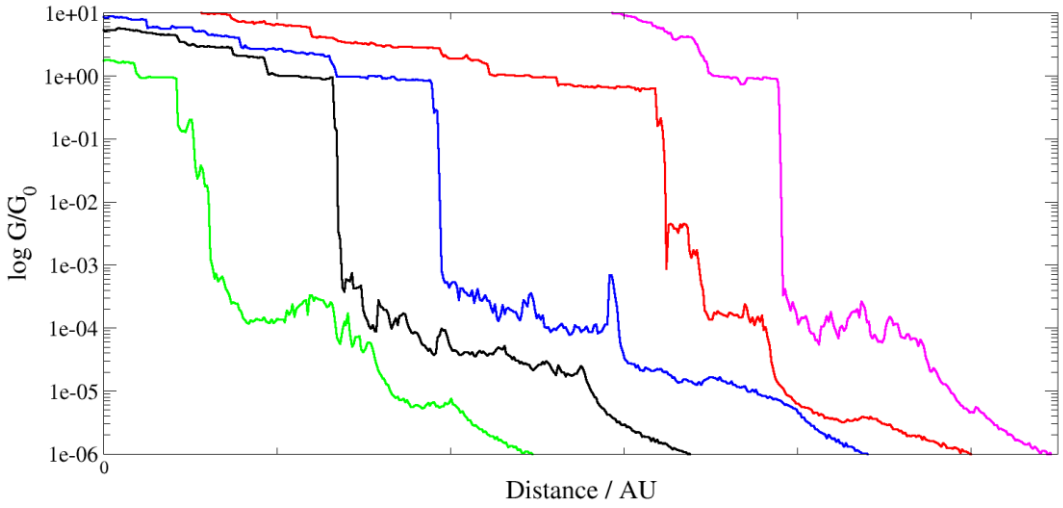

Fig. 30: Exemplary breaking curves from STM-BJ experiment of [9]helicene **15**.

Similarly, a logarithmic 1D histogram (Fig. 31) shows a diffusive peak with maximum at $1 \cdot 10^{-4}$ G/G_0, which spreads over more than three orders of magnitude. The oxygen-bound state peak, in this case, is probably below our detection level (10^{-6} G/G_0). The single-molecule conductance of [9]helicene **15** was also confirmed by theoretical calculations using QuantumWise ATK (for more details see *Experimental section*). The obtained value of $9 \cdot 10^{-5}$ G/G_0 (Fig. 31) nicely matches to the maximum of the conductance peak from experiment ($1 \cdot 10^{-4}$ G/G_0).

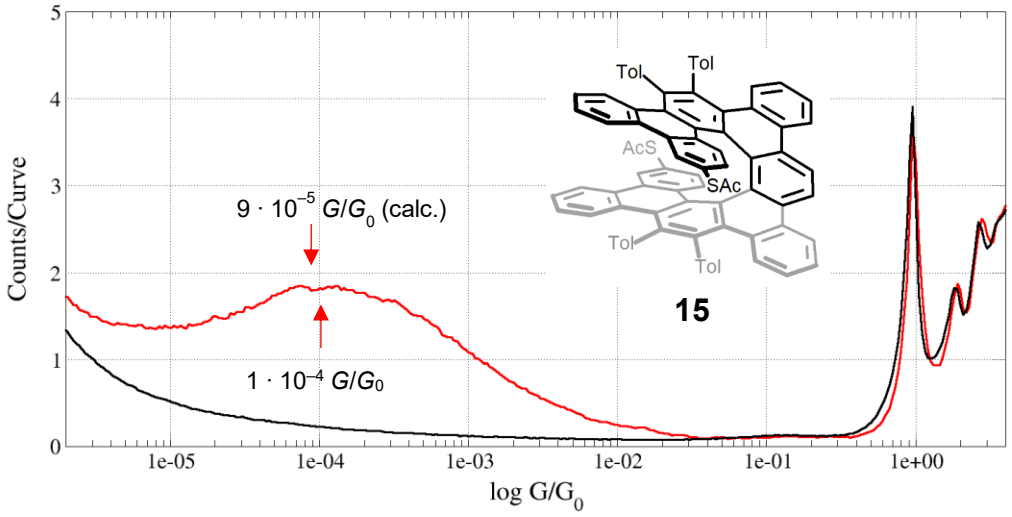

Fig. 31: Logarithmic conductance histogram of [9]helicene **15** (red, inset structure) and blank gold sample (black) with the denoted experimental and calculated conductance value.

In a 2D histogram (Fig. 32), a wide plateau appears, which ends roughly at 11.5 Å (white bar in Fig. 32). Although the DFT calculations predicted the higher sulfur-sulfur distance of 13.37 Å, the results are not unrealistic. The molecules tend to stick to the surface and so the effective molecular length taken from the 2D histogram is expected to be rather lower. Slightly higher distance between the sulfur atoms was also obvious from the X-ray diffraction experiment (12.54 Å, Fig. 33). Though the obtained distances do not match precisely, their similarity proves presence of only one molecule in a molecular junction.

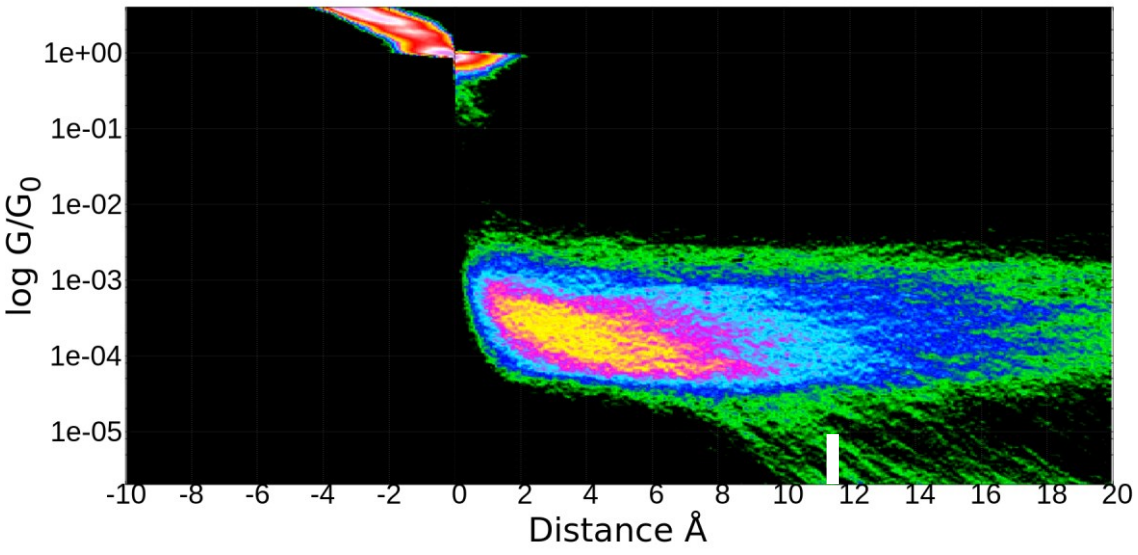

Fig. 32: 2D conductance-distance histogram of [9]helicene **15**.

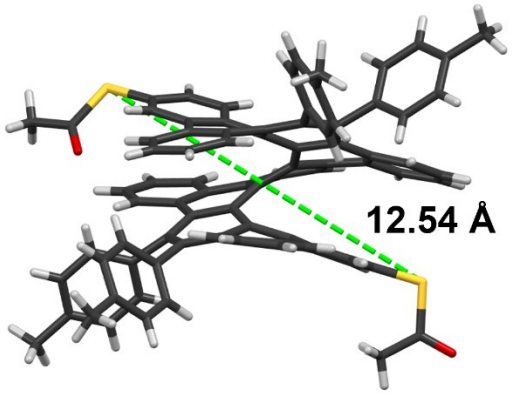

15

Fig. 33: X-ray crystal structure of [9]helicene **15** with the depicted sulfur-sulfur distance.

3.4.5 Conductance comparison of helicenes 14 and 15

Finally, the single-molecule conductance of target [5]- and [9]helicene were compared to each other. [5]Helicene **14** was found to be more conductive with higher conductance peak maximum at $1 \cdot 10^{-3}$ G/G_0, whereas [9]helicene **15** showed a conductance peak maximum at $1 \cdot 10^{-4}$ G/G_0. This decrease of conductance is in an agreement with a general trend of exponentially decreasing conductance with increasing length of a molecular wire.

However, in case of helicenes, the conductance decays much more slowly. For example, the same one order drop in conductance, achieved by prolonging the helicene backbone of four more aromatic rings, is equivalent to addition of only two ethylene units.[75] It can probably be ascribed to aromaticity and an additional interaction of wide aromatic parts of a helicene with a metal surface.

The conductance data obtained for helicenes **14** and **15** may be used to predict conductance of [7]helicene **37** (Fig. 33b). According to the exponential decay, a conductance value of approx. $3 \cdot 10^{-4}$ G/G_0 would be expected for [7]helicene **37**. Anyway, conductance of another [7]helicene **36** (Fig. 33b). was found to be $1 \cdot 10^{-2}$ G/G_0,[41] what is even higher than value for [5]helicene **14** (Fig. 33a). However, their structures are quite different. For example, [7]helicene **36** bears the acetylsulfanyl anchoring groups at adjacent carbon atoms relatively to [7]helicene **37**, and so their conductance may differ.

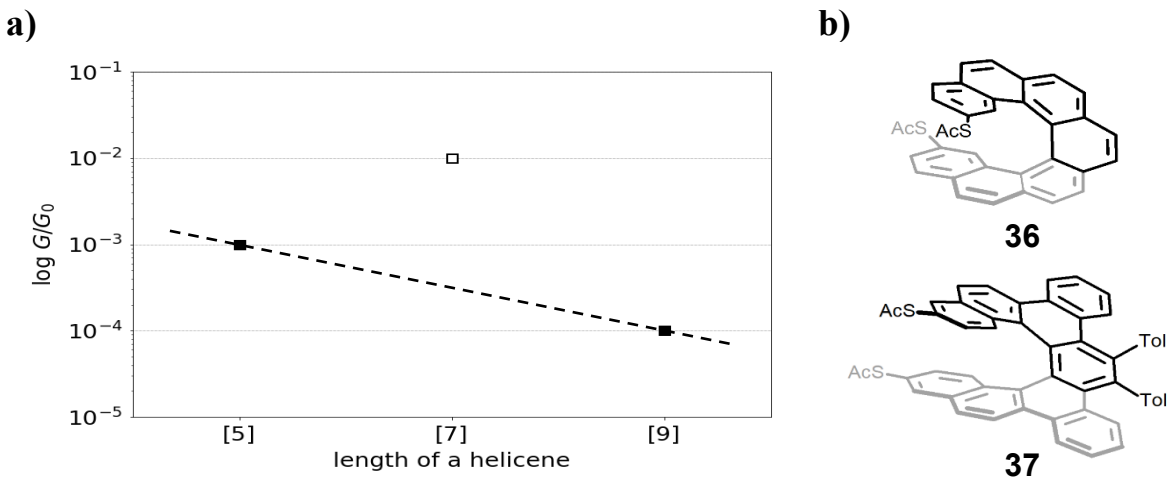

Fig. 33: a) Logarithmic conductance plot of [5]helicene **14** and [9]helicene **15** (full squares), and [7]helicene **36** (hollow square)[41] and b) structures of [7]helicenes **36** and **37**.

4 Conclusions

Two target molecules, [5]helicene **14** and [9]helicene **15** (Fig. 34), were prepared in good to excellent yields. [2+2+2] Cyclotrimerization of [5]helicene **14** was found to proceed in a higher yield than that of [9]helicene **15**, probably due to the smaller sterical hindrance. Above that, [9]helicene **15** was resolved into enantiomers to enable STM-BJ experiments on them, for example, for future studies of the CISS effect. Also, biphenyl **16** was designed and prepared as a model compound of similar length to [5]helicene **14**.

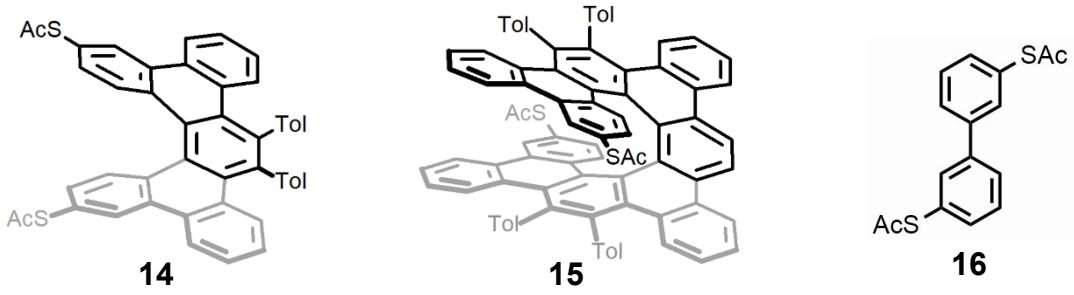

Fig. 34: Target acetylsulfanyl [*n*]helicenes **14** and **15** for *n* = 5 and 9, and a model compound **16**.

The single-molecule conductance of both helicenes **14** and **15**, and model compound **16** were measured in STM-BJ device, once the introductory experiments proved reliability of the method. Comparing the results showed a higher conductance of the shorter [5]helicene **14** than that of the longer [9]helicene **15**, what is in agreement with a general trend of decreasing conductance with increasing length of a molecular wire. Next, the conductance histogram of [5]helicene **14** contains two peaks, which are attributed to sulfur or oxygen-bound species, as was already observed elsewhere.[70] The conductance peak of [9]helicene **15** is more diffusive because of the greater conformational freedom on the longer helical backbone.

The theoretical calculations were used to confirm the conductance of both helicenes **14** and **15**. While the theoretically calculated conductance and the experimentally observed value were almost identical for [9]helicene **15**, the results for [5]helicene **14** were only in order of magnitude agreement.

The effective length of molecular junctions was taken from the 2D conductance-length histograms. The biphenyl **16** proved to be a good choice as a model, since its effective molecular length was only slightly lower than that of [5]helicene **14**. Furthermore, the effective length of both helicenes **14** and **15** was correlated with the sulfur-sulfur distance obtained from DFT

calculations or X-ray diffraction experiments. In both cases, X-ray diffraction afforded values closer to the actual effective length from STM-BJ measurements than DFT calculations.

5 Experimental section

5.1 General information

Melting points were determined on Mikro-Heiztisch Polytherm A (Hund, Wetzlar) apparatus and are uncorrected.

The NMR spectra were measured on Bruker Advance III HD 400, 500, and 600 instruments, respectively. The ^{1}H NMR spectra were measured at 400.13 MHz, 499.88 MHz, and 600.13 MHz, the ^{13}C NMR spectra at 100.61 MHz, 125.71 MHz, and 150.90 MHz in $CDCl_3$. For referencing the spectra, the residual chloroform signal was used (δ 7.26 ppm for ^{1}H and δ 77.16 ppm for ^{13}C NMR spectra). The chemical shifts are given in δ-scale, the coupling constants *J* are given in Hz. For the assignment of both the ^{1}H and ^{13}C NMR spectra of the key compounds, homonuclear 2D-H,H-COSY and heteronuclear 2D-H,C-HSQC, and 2D-H,C-HMBC experiments were performed by Dr. Radek Pohl.

The UV-Vis absorption, fluorescence, and ECD spectra were measured on a spectropolarimeter Jasco 1500 equipped with a fluorescence emission monochromator (FMO522) and a separate fluorescence emission detector (FDT-538). The UV-Vis absorption and the ECD spectra were obtained in the range of wavelengths of 225–500 nm. The measurements were carried out in a 10 mm quartz sample cell with scan-speed of 20 nm/min, response-time of 4 s and a standard device sensitivity. After baseline correction, the UV-Vis spectra were expressed in terms of the molar extinction coefficient (ε) and the ECD spectra in the molar extinction coefficient difference ($\Delta\varepsilon$). The fluorescence spectra were measured with the constant slit widths of an emission and excitation monochromator (10 nm, 5 nm). All samples were the 10^{-4} M $CHCl_3$ solutions and the pure $CHCl_3$ was used as a baseline.

The IR spectra were measured in a KBr cell in a $CHCl_3$ solution on Nicolet 6700 FT-IR spectrometer (Thermo Fisher Scientific, USA) equipped with a standard mid-IR source, a KBr beam-splitter and a DTGS detector and with a cell compartment purged by dry nitrogen. Optical rotations were measured in $CHCl_3$ using an Autopol IV instrument (Rudolph Research Analytical).

The low resolution ESI mass spectra were recorded on Q-Tof micro (Waters) and the high resolution ESI mass spectra and APCI spectra using the Orbitrap mass analyzer (LTQ

Orbitrap XL, Thermo Fisher Scientific). The MALDI-TOF spectra were measured on UltrafleXtremeTM MALDI-TOF/TOF mass spectrometer (Bruker Daltonics, Germany).

Crystallographic data were collected on Bruker D8 VENTURE Kappa Duo PHOTON 100 by IμS micro-focus sealed tube MoKα radiation (λ = 0.71073 Å) at a temperature of 120 K. The structures were solved by direct methods (XP)[76] or methods (XT) and refined by full matrix least squares based on F^2 (SHELXL2014 or SHELXL2018).[77] The hydrogen atoms on carbon were fixed into idealized positions (riding model) and assigned a temperature factor $H_{iso}(H) = 1.0\ U_{eq}$ (pivot atom). All crystallographic measurements were performed by Dr. Ivana Císařová.

TLC was performed on Silica gel 60 F_{254}-coated aluminium sheets (Merck) and spots were detected by a solution of $Ce(SO_4)_2 \cdot 4H_2O$ (1%) and $H_3P(Mo_3O_{10})_4$ (2%) in sulfuric acid (10%). The flash chromatography was performed on Silica gel 60 (0.040-0.063 mm, Merck) or on Biotage® KP-C18-HS cartridges using the Isolera One HPFC system (Biotage, Inc.).

DIPA was distilled from calcium hydride under nitrogen; THF was freshly distilled from sodium/benzophenone under nitrogen; toluene and mesitylene were distilled from sodium under nitrogen. HPLC-grade NMP was distilled under nitrogen. Solvents for enantiomer separation were of an HPLC-grade. Otherwise, all the commercially available solvents, catalysts, and reagent grade materials were used as received. 4-Iodotoluene, 2-bromo-1-iodobenzene **23**, 2-bromo-4-chloro-1-iodobenzene **19**, 3-chloro-1-iodobenzene **30**, and 3-chlorophenylboronic acid **32** were purchased.

Arylated acetylene **20** was synthesized according to the literature procedure.[65] Tetrayne **26** was prepared by Martin McLaughlin (University of Bristol, UK), stilbene **34** by Ing. Arnošt Seidler[66] and [5]helicene **33** by Dr. Jindřich Nejedlý.[41]

5.2 Synthesis

1-Bromo-2-[(4-methylphenyl)ethynyl]benzene 24[78]

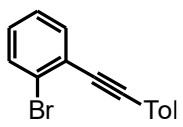

A dry Schlenk flask was charged with 2-bromo-1-iodobenzene **23** (2.30 mL, 17.9 mmol), $Pd(PPh_3)_2Cl_2$ (126 mg, 0.179 mmol, 1 mol%), and CuI (68 mg, 0.36 mmol, 2 mol%). The flask was purged with nitrogen. Distilled DIPA (100 mL) was added and after degassing with three freeze-pump-thaw cycles, a reaction mixture was cooled down to 0 °C. TMSA (2.60 mL, 18.8 mmol, 1.05 eq.) was added dropwise and the reaction mixture was stirred overnight. A dense white precipitate appeared. A TBAF · $3H_2O$ solution in THF (2.5 M, 10.75 mL, 27 mmol, 1.5 eq.) was added dropwise and stirred at room temperature for 30 min.

4-Iodotoluene (11.72 g, 53.76 mmol, 3.0 eq.), $Pd(PPh_3)_2Cl_2$ (126 mg, 0.179 mmol, 1 mol%), and CuI (68 mg, 0.36 mmol, 2 mol%) all dissolved in DIPA (30 mL) and toluene (30 mL) were added at once at 0 °C. The reaction mixture was then degassed once more with a freeze-pump-thaw cycle and stirred at room temperature for 12 h. TLC analysis showed the full conversion of the starting material.

The reaction mixture was filtered through a short plug of silica (frit S2, toluene) and the solvents were evaporated *in vacuo*. After dilution with cyclohexane (1:1), the crude mixture was separated by column chromatography (cyclohexane). Halide **24** (4.56 g, 96 %) was obtained as a white crystalline solid.

^1H and ^{13}C NMR spectra were in agreement with the published data.[78]

{2-[(4-Methylphenyl)ethynyl]phenyl}boronic acid 22[79]

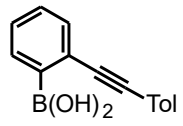

A dry Schlenk flask was charged with halide **24** (3.56 g, 13.1 mmol) dissolved in THF (93 mL). After cooling down to –78 °C, *n*-BuLi (1.6 M solution in hexanes, 10.70 mL, 17 mmol, 1.3 eq.) was added dropwise. After 45 min of stirring at the same temperature, triisopropylborate (7.55 mL, 32.8 mmol, 2.50 eq.) was added in one portion and the reaction mixture was left to reach room temperature. After 30 min, the reaction was quenched with HCl (1 M, 20 mL) and stirred for 1 h. The organic and aqueous phases were separated. The aqueous phase was extracted with ether (3 x 15 mL), the organic

fractions were combined. Then, the organic phase was extracted with brine (1 x 100 mL), dried over anhydrous magnesium sulfate, filtered, and evaporated *in vacuo*. Column chromatography (hexane:ether 95:5 to 75:25) afforded boronic acid **22** (2.92 g, 94 %) as a white crystalline solid.

^{1}H and ^{13}C NMR spectra were in agreement with the published data.[79]

1,1'-Ethyne-1,2-diylbis(2-bromo-4-chlorobenzene) 20[65]

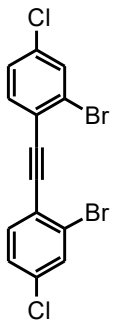

A dry Schlenk flask was charged with 2-bromo-4-chloro-1-iodobenzene **19** (1.87 g, 5.89 mmol), $Pd(PPh_3)_4$ (681 mg, 0.589 mmol, 10 mol%), CuI (224 mg, 1.18 mmol, 20 mol%), and purged with nitrogen. DIPA (90 mL) was added and the mixture was degassed using three freeze-thaw-pump cycles. The reaction mixture was stirred under acetylene atmosphere at 55 °C for 20 h. Then, the solvent was evaporated *in vacuo* and flash chromatography (hexane:chloroform 85:15) afforded arylated acetylene **20** (1.02 g, 86 %) as a white amorphous solid.

^{1}H and ^{13}C NMR spectra were in agreement with the published data.[65]

2,2'-Ethyne-1,2-diylbis{5-chloro-2'-[(4-methylphenyl)ethynyl]biphenyl} 21

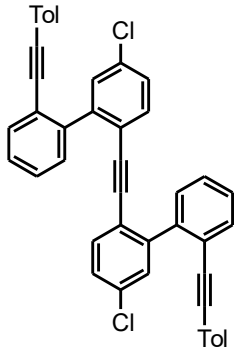

A Schlenk flask was charged with arylated acetylene **20** (1.00 g, 2.47 mmol), boronic acid **22** (1.75 g, 7.41 mmol, 3.0 eq.), $Pd(PPh_3)_2Cl_2$ (173 mg, 0.247 mmol, 10 mol%), K_2CO_3 (1.02 g, 7.41 mmol, 3.0 eq.) and purged with nitrogen. Toluene (27 mL), demineralized water (7 mL), and *n*-PrOH (27 mL) were added and the mixture was bubbled with nitrogen for 10 min. The reaction mixture was then stirred at 90 °C for 3 h. The solvents were evaporated *in vacuo* and flash chromatography (hexane:chloroform 20:80 to 65:35) afforded triyne **21** (1.17 g, 75 %) as an orange-brown amorphous solid.

^{1}H NMR (400 MHz, $CDCl_3$): δ 7.63 – 7.58 (m, 2H), 7.54 (d, *J* = 2.1, 2H), 7.39 – 7.27 (m, 6H), 7.25 – 7.10 (m, 8H), 7.08 – 7.02 (m, 4H), 2.31 (s, 6H) ppm.

^{13}C NMR (101 MHz, $CDCl_3$): δ 144.0, 141.3, 138.4, 133.6, 133.5, 132.2, 131.4, 130.7, 130.3, 129.1, 128.0, 127.7, 127.6, 122.8, 121.3, 120.3, 93.4, 91.9, 88.0, 21.6 ppm.

IR ($CHCl_3$): 3085 vw, 3064 w, 2959 w, 2925 m, 2857 w, 2217 w, 1598 w, 1588 w, 1564 vw, 1549 vw, 1512 s, 1498 m, 1472 m, 1447 w, 1397 m, 1288 w, 1262 w, 1182 w, 1127 w, 1117 w, 1103 m, 1094 m, 1044 w, 1019 m, 950 w, 889 w, 870 m, 819 vs cm^{-1}.

APCI MS: 627 ($[M+H]^+$).

HR APCI MS: calculated for $C_{44}H_{29}{}^{35}Cl_2$ 627.1641, found 627.1648.

3,12-Dichloro-7,8 -ditolyl-dibenzo[*f,l*]pentahelicene 25

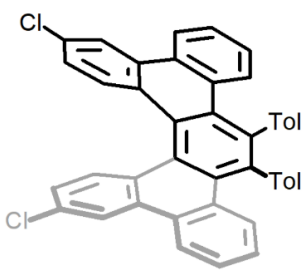

A dry Schlenk flask was charged with triyne **21** (1.17 g, 1.86 mmol) and $Ni(PPh_3)_2(CO)_2$ (715 mg, 1.12 mmol, 60 mol%). Toluene (117 mL) was added and bubbled with nitrogen for 10 min. The reaction mixture was stirred at 140 °C for 1.5 h. The solvent was evaporated *in vacuo*. Flash chromatography (hexane:chloroform 75:25) and reverse phase flash chromatography (MeOH:ACN 75:25) afforded [5]helicene **25** (530 mg, 45 %) as an orange-brown crystalline solid.

M.p.: >300 °C (MeOH:ACN).

^{1}H NMR (400 MHz, $CDCl_3$): δ 8.46 – 8.40 (m, 4H), 8.00 (d, *J* = 8.9, 2H), 7.47 (ddd, *J* = 8.2, 7.0, 1.2, 2H), 7.39 (dd, *J* = 8.6, 1.1, 2H), 7.15 (dd, *J* = 8.9, 2.2, 2H), 7.06 (ddd, *J* = 8.4, 7.0, 1.3, 2H), 7.03 – 6.94 (m, 4H), 6.91 (dd, *J* = 7.9, 1.8, 2H), 6.76 (dd, *J* = 7.8, 1.9, 2H), 2.33 (s, 6H) ppm.

^{13}C NMR (101 MHz, $CDCl_3$): δ 139.2, 138.8, 136.1, 133.0, 132.8, 131.8, 131.6, 131.4, 130.7, 130.5, 130.3, 129.52, 129.48, 129.1, 128.9, 127.9, 126.61, 126.60, 126.2, 123.7, 123.2, 22.1 ppm.

IR ($CHCl_3$): 3076 w, 3051 w, 3029 w, 3001 m, 2954 w, 2924 w, 2869 w, 1596 s, 1576 vw, 1565 w, 1519 w, 1511 s, 1487 s, 1438 vs, 1411 m, 1386 w, 1363 w, 1341 w, 1183 w, 1113 s, 1095 w, 1056 w, 1022 m, 875 m, 844 m, 831 s, 822 m, 803 w, 639 w, 467 w, 427 w cm^{-1}.

UV-Vis ($CHCl_3$): λ_{max} (log ε) = 242 (5.06), 296 (4.80), 327 (4.82), 375 nm (4.18).

Fluorescence ($CHCl_3$, λ_{exc} 375 nm): λ_{max} (I_r) 456 nm (0.806).

MALDI MS: 626 ($[M]^+$).

HR MALDI MS: calculated for $C_{44}H_{28}{}^{35}Cl_2$ 626.1563, found 626.1576.

3,12-Bis(acetylsulfanyl)-7,8 -ditolyl-dibenzo[*f*,*l*]pentahelicene 14

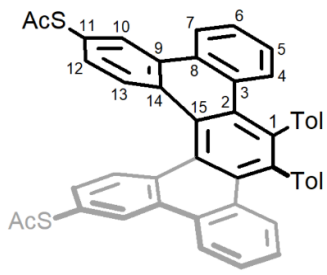

A dry Schlenk flask was charged with freshly distilled NMP (5 mL), sodium (247 mg, 10.8 mmol, 45.0 eq.), and DMDS (735 µL, 8.27 mmol, 35.0 eq.). The mixture was sonicated to full dissolution of sodium. [5]helicene **25** (150 mg, 0.239 mmol) was added in degassed NMP (5 mL). The apparatus was attached to an emergency bleach bath. Then, the reaction mixture was refluxed in a metallic heatblock at 200 °C for 3 h. Once cooled down to 0 °C, AcCl (1.05 mL, 14.7 mmol, 62.0 eq.) was added. The reaction mixture was stirred at room temperature for 2 h and then poured into an ice-filled separation funnel for extraction with DCM (3 x 15 mL). The combined organic phases were extracted with brine (3 x 50 mL), dried over anhydrous magnesium sulfate, filtered, and evaporated *in vacuo*. Flash chromatography (cyclohexane:DCM 60:40 to 40:60) yielded [5]helicene **14** (150 mg, 89 %) as a yellow crystalline solid.

M.p.: 265 – 267 °C (DCM:ACN).

^{1}H NMR (600 MHz, $CDCl_3$): δ 8.54 (d, $J_{10,12}$ = 1.9, 2H, H-10); 8.48 (dd, $J_{7,6}$ = 8.2, $J_{7,5}$ = 1.5, 2H, H-7); 8.15 (d, $J_{13,12}$ = 8.6, 2H, H-13); 7.47 (ddd, $J_{6,7}$ = 8.2, $J_{6,5}$ = 7.0, $J_{6,4}$ = 1.2, 2H, H-6); 7.39 (dd, $J_{4,5}$ = 8.5, $J_{4,6}$ = 1.2, 2H, H-4); 7.21 (dd, $J_{12,13}$ = 8.6, $J_{12,10}$ = 1.9, 2H, H-12); 7.05 (ddd, $J_{5,4}$ = 8.5, $J_{5,6}$ = 7.0, $J_{5,7}$ = 1.5, 2H, H-5); 7.02 (dd, $J_{m,o}$ = 7.8, $J_{m,m}$ = 2.0, 2H, H-*m*-Tol); 6.97 (dd, $J_{o,m}$ = 7.8, $J_{o,o}$ = 2.0, 2H, H-*o*-Tol); 6.92 (dd, $J_{m,o}$ = 7.8, $J_{m,m}$ = 2.0, 2H, H-*m*-Tol); 6.77 (dd, $J_{o,m}$ = 7.8, $J_{o,o}$ = 2.0 , 2H, H-*o*-Tol); 2.47 (s, 6H, CH_3CO); 2.34 (s, 6H, CH_3-Tol) ppm.

^{13}C NMR (151 MHz, $CDCl_3$): δ 194.0 (CH_3**C**O); 139.0 (C-*i*-Tol); 138.9 (C-1); 135.9 (C-*p*-Tol); 132.2 (C-14); 132.0 (CH-13); 131.5, 131.7 (CH-*o*-Tol); 131.3 (CH-12); 130.8 (C-8); 130.5 (C-9); 130.3 (C-3); 129.9 (C-2); 129.8 (CH-10); 129.3 (CH-4); 128.7, 128.9 (CH-*m*-Tol); 128.1 (C-15); 126.4 (CH-6); 126.3 (C-11); 125.8 (CH-5); 123.3 (CH-7); 30.3 (**C**H_3CO); 21.3 (CH_3-Tol) ppm.

IR ($CHCl_3$): 3051 w, 3002 m, 2925 m, 2855 w, 1703 vs, 1595 w, 1516 w, 1509 m, 1484 w, 1439 m, 1408 w, 1385 w, 1354 w, 1125 s, 1112 s, 1056 w, 1022 m, 1001 w, 951 m, 909 m, 886 w, 877 w, 843 w, 835 m, 831 m, 822 w, 638 w, 463 w cm^{-1}.

UV-Vis ($CHCl_3$): λ_{max} (log ε) = 254 (5.47), 300 (5.35), 333 (5.44), 382 nm (4.90).

Fluorescence ($CHCl_3$, λ_{exc} 380 nm): λ_{max} (I_r) 460 nm (2.67).

APCI MS: 707 ($[M+H]^+$).

HR APCI MS: calculated for $C_{48}H_{35}O_2S_2$ 707.2073, found 707.2078.

({2',3'-Bis[(2-bromo-4-chlorophenyl)ethynyl]-1,1':4',1''-terphenyl-2,2''-diyl}diethyne-2,1-diyl)bis[tris(1-methylethyl)silane] 27

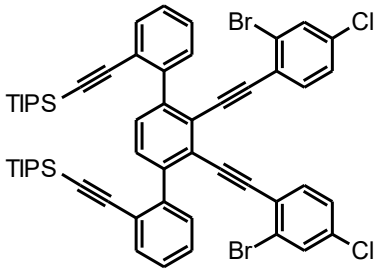

A dry Schlenk flask was charged with tetrayne **26** (1.46 g, 2.28 mmol), 2-bromo-4-chloro-1-iodobenzene **19** (2.17 g, 6.83 mmol, 3.0 eq.), $Pd(PPh_3)_2Cl_2$ (80 mg, 0.11 mmol, 5.0 mol%), and CuI (44 mg, 0.23 mmol, 10 mol%). The flask was three-times purged with nitrogen. DIPA (87 mL) and toluene (22 mL) were added via septum. The reaction mixture was degassed with three freeze-pump-thaw cycles and stirred overnight. A grey precipitate was formed while TLC showed full conversion. The reaction mixture was filtered through a short plug of silica (toluene) and solvents were evaporated *in vacu*o. Flash chromatography (hexane:chloroform 95:5 to 90:10) afforded tetrayne **27** (2.00 g, 86 %) as a yellowish amorphous solid.

^{1}H NMR (400 MHz, $CDCl_3$): δ 7.61 (dt, *J* = 7.5, 1.1, 2H), 7.48 (d, *J* = 1.9, 2H), 7.41 (s, 2H), 7.40 – 7.36 (m, 4H), 7.36 – 7.30 (m, 2H), 7.19 – 7.10 (m, 4H), 0.98 (s, 42H) ppm.

^{13}C NMR (101 MHz, $CDCl_3$): δ 143.4, 143.2, 134.4, 134.3, 132.9, 132.2, 129.9, 129.8, 128.2, 127.6, 127.2, 125.6, 125.2, 124.7, 123.6, 105.8, 94.5, 93.9, 93.5, 18.8, 11.4 ppm.

IR ($CHCl_3$): 3091 vw, 3064 w, 2958 m, 2944 s, 2927 m, 2891 m, 2865 s, 2156 w, 1602 w, 1581 w, 1542 vw, 1474 vs, 1461 sh, m, 1439 w, 1435 w, 1383 w, 1374 w, 1367 w, 1245 vw, 1115 vw, 1098 m, 1068 w, 1043 w, 1033 w, 1018 w, 997 w, 919 vw, 883 m, 873 w, 843 w, 829 m, 802 w, 708 m, 678 m, 639 m, 626 w, 560 w, 522 vw, 438 vw cm^{-1}.

MALDI MS: 1037 ($[M+Na]^+$).

HR MALDI MS: calculated for $C_{56}H_{58}{}^{79}Br_2{}^{35}Cl_2Si_2Na$ 1037.1713, found 1037.1731.

{[2',3'-Bis({5-chloro-2'-[(4-methylphenyl)ethynyl]biphenyl-2-yl}ethynyl)-1,1':4',1''-terphenyl-2,2''-diyl]diethyne-2,1-diyl}bis[tris(1-methylethyl)silane] 28

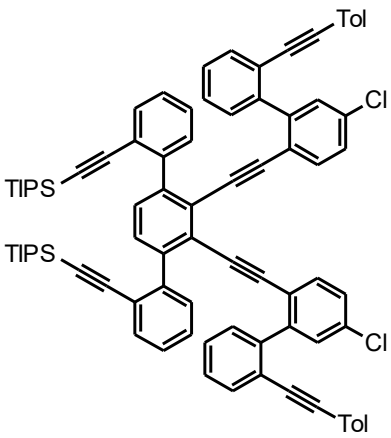

A Schlenk flask was charged with tetrayne **27** (2.00 g, 1.97 mmol), boronic acid **22** (1.40 g, 5.92 mmol, 3.0 eq.), $Pd(PPh_3)_2Cl_2$ (111 mg, 0.157 mmol, 8 mol%), and K_2CO_3 (818 mg, 5.92 mmol, 3.0 eq.), and purged with nitrogen. Toluene (21 mL), *n*-PrOH (21 mL), and demineralized water (5 mL) were added via septum. The reaction mixture was bubbled with nitrogen gas for 10 min, then heated to 90 °C and stirred for 3 h. The reaction mixture was diluted with water (15 mL) and extracted with chloroform (3 x 20 mL). The combined organic phases were collected, dried over anhydrous magnesium sulfate, filtered, and evaporated *in vacuo*. Flash chromatography (hexane:chloroform 90:10) afforded hexayne **28** (1.93 g, 80 %) as a brown amorphous solid.

^{1}H NMR (400 MHz, $CDCl_3$): δ 7.56 (d, J = 2.2, 2H), 7.50 (dd, J = 7.5, 1.6, 2H), 7.41 – 7.35 (m, 2H), 7.29 – 6.99 (m, 26H), 2.33 (s, 6H), 0.95 (s, 42H) ppm.

^{13}C NMR (101 MHz, $CDCl_3$): δ 143.2, 142.9, 142.6, 140.7, 138.4, 134.8, 133.0, 132.8, 132.3, 131.4, 130.9, 130.2, 129.7, 129.5, 129.2, 128.4, 127.9, 127.74, 127.65, 127.41, 127.35, 125.4, 125.3, 122.9, 122.0, 121.3, 120.4, 106.0, 94.8, 94.2, 93.1, 91.8, 88.4, 21.7, 18.7, 11.4 ppm.

IR ($CHCl_3$): 3063 w, 3010 m, 2968 s, 2958 s, 2944 vs, 2924 s, 2891 m, 2865 vs, 2757 vw, 2725 vw, 2216 vw, 2156 m, 1904 vw, 1597 w, 1585 w, 1565 vw, 1547 vw, 1512 m, 1494 m, 1467 vs, 1446 m, 1405 w, 1389 w, 1383 w, 1366 w, 1290 w, 1182 w, 1161 w, 1113 w, 1104 w, 1096 m, 1073 w, 1064 w, 1044 w, 1033 w, 1019 m, 996 m, 949 w, 919 w, 883 m, 858 w, 843 m, 828 s, 819 s, 679 m, 662 m cm^{-1}.

MALDI MS: 1240 ($[M+H]^+$), 1262 ($[M+Na]^+$).

HR MALDI MS: calculated for $C_{86}H_{81}{}^{35}Cl_2Si_2$ 1239.5248, found 1239.5258; for $C_{86}H_{80}{}^{35}Cl_2Si_2Na$ 1261.5068, found 1261.5083.

2',3'-Bis({5-chloro-2'-[(4-methylphenyl)ethynyl]biphenyl-2-yl}ethynyl)-2,2''-bis[(4-methylphenyl)ethynyl]-1,1':4',1''-terphenyl 17

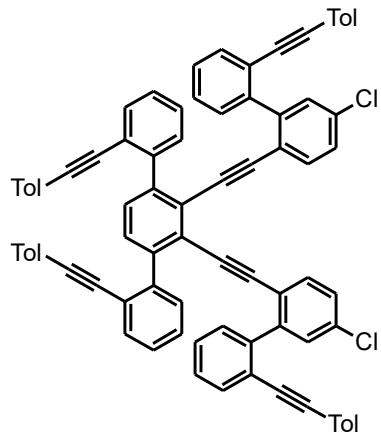

A Schlenk flask (solution A) was charged with hexayne **28** (1.93 g, 1.56 mmol) and purged with nitrogen. It was dissolved in toluene (30 mL) and a THF solution of TBAF · $3H_2O$ (1.0 M, 4.65 mL, 4.7 mmol, 3.0 eq.) was added dropwise via septum. After 20 min, TLC showed full conversion. Another Schlenk flask (solution B) was charged with $Pd(PPh_3)_2Cl_2$ (55 mg, 0.078 mmol, 5 mol%), CuI (30 mg, 0.16 mmol, 10 mol%), and 4-iodotoluene (814 mg, 3.73 mmol, 2.4 eq.), and purged with nitrogen. DIPA (10 mL) and toluene (20 mL) were added and both solutions A and B were degassed using three freeze-thaw-pump cycles. Then, the solution A was cannulated dropwise to the solution B and stirred at room temperature for 20 h. The reaction mixture was filtered through a short plug of silica (toluene) and column chromatography (hexane:chloroform 65:35) afforded hexayne **17** (1.35 g, 78 %) as a brown-yellow amorphous solid.

^{1}H NMR (400 MHz, $CDCl_3$): δ 7.62 – 7.53 (m, 4H), 7.44 (s, 2H), 7.36 – 7.27 (m, 6H), 7.25 – 7.13 (m, 8H), 7.13 – 7.04 (m, 12H), 7.01 (td, J = 7.5, 1.2, 2H), 6.94 – 6.83 (m, 6H), 2.32 (s, 6H), 2.25 (s, 6H) ppm.

^{13}C NMR (101 MHz, $CDCl_3$): δ 134.6, 132.3, 132.1, 131.4, 131.4, 131.0, 130.5, 130.1, 129.6, 129.2, 129.0, 127.8, 127.71, 127.65, 127.4, 95.2, 93.4, 93.2, 91.9, 88.5, 88.5, 21.7, 21.6 ppm.

IR ($CHCl_3$): 3062 w, 3010 w, 2957 w, 2924 w, 2858 w, 2216 w, 1906 vw, 1597 w, 1584 w, 1546 w, 1512 s, 1495 w, 1468 m, 1444 w, 1441 sh,w, 1406 w, 1392 w, 1262 vw, 1182 w, 1162 vw, 1118 w, 1104 w, 1095 w, 1044 w, 1019 m, 948 w, 906 w, 890 w, 859 w, 834 w, 819 vs, 655 vw, 541 w cm^{-1}.

MALDI MS: 1106 ($[M]^+$).

HR MALDI MS: calculated for $C_{82}H_{52}{}^{35}Cl_2$ 1106.3441, found 1106.3455.

3,20-Dichloro-7,8,15,16-tetratolyl-tetrabenzo[*f*,*l*,*r*,*x*]nonahelicene 18

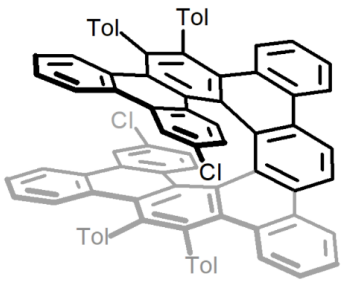

A Schlenk flask was charged with hexayne **17** (1.38 g, 1.25 mmol) and $Ni(PPh_3)_2(CO)_2$ (478 mg, 0.747 mmol, 60 mol%). Toluene (75 mL) was added, the reaction mixture was bubbled with nitrogen within 10 min and stirred at 140 °C for 1.5 h. The solvent was evaporated and flash chromatography (cyclohexane:chloroform 70:30) afforded [9]helicene **18** (560 mg, 41 %) as a brown crystalline solid.

M.p.: 262 – 264 °C (pentane).

^{1}H NMR (400 MHz, $CDCl_3$): δ 8.84 (s, 2H), 8.61 (dd, *J* = 8.2, 1.4, 2H), 8.44 (dd, *J* = 8.5, 1.3, 2H), 8.27 (d, *J* = 2.2, 2H), 7.55 – 7.45 (m, 4H), 7.40 (dd, *J* = 8.6, 1.2, 2H), 7.33 (td, *J* = 8.1, 1.1, 2H), 7.15 – 6.93 (m, 8H), 6.73 – 6.65 (m, 2H), 6.62 – 6.42 (m, 6H), 6.31 (dd, *J* = 8.6, 1.1, 2H), 6.06 (ddd, *J* = 13.3, 7.7, 1.9, 4H), 5.96 (dd, *J* = 8.8, 2.1, 2H), 2.33 (s, 6H), 2.21 (s, 6H) ppm.

^{13}C NMR (101 MHz, $CDCl_3$): δ 140.1, 139.8, 139.0, 138.6, 135.5, 135.4, 133.8, 132.9, 132.0, 130.9, 130.80, 130.76, 130.7, 130.5, 130.1, 129.91, 129.87, 129.7, 129.6, 129.5, 129.3, 129.1, 128.8, 128.7, 128.5, 128.3, 128.2, 127.3, 126.6, 126.3, 125.7, 125.6, 125.4, 124.2, 122.3, 122.1, 121.8, 121.3, 21.4, 21.3 ppm.

IR ($CHCl_3$): 3084 m, 3052 m, 3005 s, 2925 s, 2867 m, 2854 m, 1950 vw, 1901 w, 1802 vw, 1595 m, 1576 vw, 1560 w, 1511 vs, 1487 m, 1461 m, 1442 m, 1438 m, 1409 w, 1383 w, 1364 w, 1308 w, 1264 w, 1157 w, 1118 m, 1112 m, 1095 w, 1057 w, 1022 m, 1001 w, 975 vw, 964 vw, 947 w, 896 w, 860 w, 842 s, 827 s, 820 s, 643 w, 613 w, 543 m, 462 w cm^{-1}.

UV-Vis ($CHCl_3$): λ_{max} (log ε) = 264 (5.14), 314 nm (4.98).

Fluorescence ($CHCl_3$, λ_{exc} 350 nm): λ_{max} (I_r) 516 nm (0.361).

MALDI MS: 1106 ($[M]^+$).

HR MALDI MS: calculated for $C_{82}H_{52}{}^{35}Cl_2$ 1106.3441, found 1106.3457.

3,20-Bis(acetylsulfanyl)-7,8,15,16-tetratolyl-tetrabenzo[*f*,*l*,*r*,*x*] nonahelicene 15

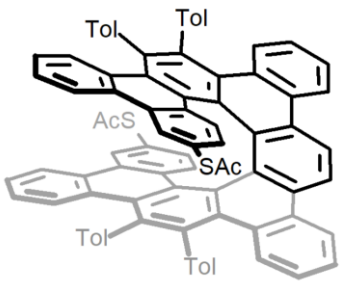

A Schlenk flask was charged with degassed NMP (5 mL), sodium (311 mg, 13.5 mmol, 50.0 eq.), and DMDS (745 µL, 8.39 mmol, 31.0 eq.) The mixture was sonicated to full dissolution of sodium. [9]helicene **18** (300 mg, 0.271 mmol) was added in degassed NMP (3 mL). The apparatus was attached to an emergency bleach bath. The reaction mixture was then refluxed in a metallic heatblock at 200 °C for 5 h. After that, the mixture was cooled down to 0 °C and AcCl (1.35 mL, 19.0 mmol, 70.0 eq.) was added. The reaction mixture was stirred at room temperature for 1 h and then poured into an ice-filled separation funnel. After extraction with DCM (3 x 10 mL), the organic phases were collected, extracted with brine (3 x 30 mL), dried over anhydrous magnesium sulfate, filtered, and evaporated *in vacuo*. Flash chromatography (cyclohexane:DCM 60:40) yielded [9]helicene **15** (186 mg, 58 %) as a brown crystalline solid.

*Chiral resolution of [9]helicene **15***

[9]Helicene **15** (80 mg) was then separated into enantiomers using the semi-preparative HPLC column Amylose SA (250 x 20 mm, 5 µm, mobile phase cyclohexane:toluene 90:10 + 1 % IPA, flow rate 1.0 mL/min). (+)-(*P*)-**15** (26 mg, 26 %, 98 % *ee*, t_R = 6.5 min) and (–)-(*M*)-**15** (32 mg, 32 %, 90 % *ee*, t_R = 11.6 min) were obtained. Enantiomeric excess was measured using

the analytical HPLC column Amylose SA (250 x 4.6 mm, 5 µm, *n*-heptane:IPA 98:2, flow rate 1.0 mL/min, $t_{R,+}$ = 7.8 min, $t_{R,-}$ = 11.2 min).

Optical Rotation ($CHCl_3$): (+)-(*P*)-**15** $[\alpha]^{20}_D$ +1563° (>99 % *ee*; *c* = 0.280); (–)-(*M*)-**15** $[\alpha]^{20}_D$ –1377° (90 % *ee*; *c* = 0.284); (–)-(*M*)-**15** $[\alpha]^{20}_D$ –1530° (recalculated for 100 % *ee*; *c* = 0.284).

M.p.: 181 – 183 °C (DCM:ACN).

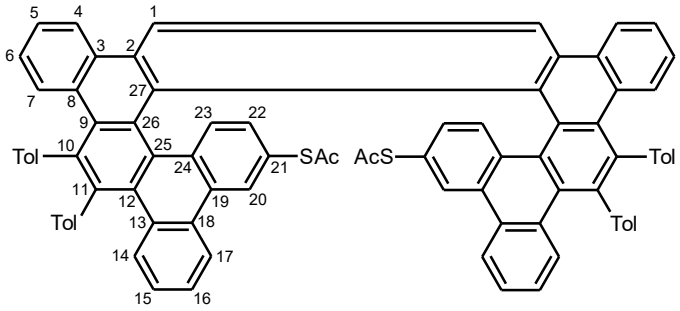

^{1}H NMR (600 MHz, $CDCl_3$): δ 8.83 (s, 2H, H-1); 8.61 (dd, $J_{4,5}$ = 8.2, $J_{4,6}$ = 1.4, 2H, H-4); 8.49 (dd, $J_{17,16}$ = 8.5, $J_{17,15}$ = 1.3, 2H, H-17); 8.40 (d, $J_{20,22}$ = 1.8, 2H, H-20); 7.47 – 7.50 (m, 4H, H-5, H-*o*-Tol-10); 7.36 (ddd, $J_{16,17}$ = 8.5, $J_{16,15}$ = 6.8, $J_{16,14}$ = 1.3, 2H, H-16); 7.33 (dd, $J_{7,6}$ = 8.5, $J_{7,5}$ = 1.2, 2H, H-7); 7.23 (dd, $J_{m,o}$ = 7.7, $J_{m,m}$ = 2.0, 2H, H-*m*-Tol-10); 7.17 (dd, $J_{o,m}$ = 7.7, $J_{o,o}$ = 2.0, 2H, H-*o*-Tol-11); 6.95 – 6.99 (m, 4H, H-6, H-*m*-Tol-11); 6.68 (dd, $J_{m,o}$ = 7.7, $J_{m,m}$ = 2.0, 2H, H-*m*-Tol-10); 6.54 – 6.57 (m, 4H, H-15, H-*m*-Tol-11); 6.50 (d, $J_{23,22}$ = 8.5, 2H, H-23); 6.33 (dd, $J_{14,15}$ = 8.5, $J_{14,16}$ = 1.3, 2H, H-14); 6.03 (dd, $J_{o,m}$ = 7.7, $J_{o,o}$ = 2.0, 2H, H-*o*-Tol-10); 6.01 (dd, $J_{o,m}$ = 7.7, $J_{o,o}$ = 2.0, 2H, H-*o*-Tol-11); 6.00 (dd, $J_{22,23}$ = 8.5, $J_{22,20}$ = 1.8, 2H, H-22); 2.32 (s, 6H, CH_3-Tol-10); 2.28 (s, 6H, CH_3CO); 2.20 (s, 6H, CH_3-Tol-11) ppm.

^{13}C NMR (151 MHz, $CDCl_3$): δ 194.54 (CH_3**C**O); 139.97 (C-*i*-Tol-10); 139.55 (C-*i*-Tol-11); 138.89 (C-11); 138.69 (C-10); 135.30 (C-*p*-Tol-10); 135.26 (C-*p*-Tol-11); 133.52 (CH-*o*-Tol-10); 132.87 (CH-*o*-Tol-11); 130.84 (C-3); 130.58 (CH-*o*-Tol-11); 130.45 (C-8); 130.42 (C-24); 130.32 (C-2); 130.29 (C-27); 130.04 (C-19); 129.93 (C-18); 129.79 (CH-23); 129.76 (CH-14); 129.65 (C-13); 129.62 (C-25); 129.45 (CH-*o*-Tol-10); 129.03 (C-12); 128.94 (C-9); 128.88 (CH-7); 128.61, 128.67 (CH-*m*-Tol-10,11); 128.53 (CH-22); 127.98 (CH-20); 127.79 (CH-*m*-Tol-10); 127.00 (CH-*m*-Tol-11); 126.33 (CH-5); 126.05 (CH-15); 125.63 (C-26); 125.60 (CH-16); 125.10 (CH-6); 125.05 (C-21); 122.19 (CH-4); 121.85 (CH-1); 121.67 (CH-17); 30.11 (**C**H_3CO); 21.26 (CH_3-Tol-10); 21.16 (CH_3-Tol-11) ppm.

IR ($CHCl_3$): 3085 w, 3051 w, 2959 m, 2926 vs, 2854 m, 1701 m, 1602 w, 1575 w, 1512 m, 1487 w, 1461 m, 1449 sh, m, 1444 m, 1405 w, 1379 w, 1364 w, 1354 w, 1308 w, 1262 m, 1159 w, 1130 sh, m, 1112 m, 1106 m, 1081 m, 1059 m, 1023 m, 1002 w, 949 w, 896 w, 878 w, 864 w, 843 w, 829 m, 820 m, 614 m cm^{-1}.

UV-Vis ($CHCl_3$): λ_{max} (log ε) = 281 (5.38), 320 nm (5.26).

Fluorescence ($CHCl_3$, λ_{exc} 325 nm): λ_{max} (I_r) 512 nm (1.02).

MALDI MS: 1186 ($[M]^+$).

HR MALDI MS: calculated for $C_{86}H_{58}O_2S_2$ 1186.3873, found 1186.3852.

3,3'-Dichlorobiphenyl 31[80]

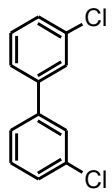

A Schlenk flask was charged with boronic acid **32** (274 mg, 1.75 mmol), $Pd(PPh_3)_2Cl_2$ (98.4 mg, 0.140 mmol, 8 mol%), and K_2CO_3 (727 mg, 5.26 mmol, 3.0 eq.), and purged with nitrogen. Toluene (20 mL), *n*-PrOH (20 mL), demineralized water (1 mL), and 3-chloro-1-iodobenzene **30** (0.35 mL, 2.8 mmol, 1.5 eq.) were added via septum. The reaction mixture was bubbled with nitrogen for 10 min, heated to 90 °C and stirred for 3 h. Then, it was diluted with water (15 mL), extracted with chloroform (20 mL). The combined organic phases were dried over anhydrous magnesium sulfate, filtered, and evaporated *in vacuo*. Flash chromatography (hexane) afforded biphenyl **31** (231 mg, 59 %) as a colorless liquid.

^1H and ^{13}C NMR spectra were in agreement with the published data.[80]

S,*S*'-Biphenyl-3,3'-diyl diethanethioate 16

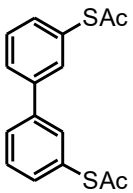

A dry Schlenk flask was charged with freshly distilled NMP (14 mL), sodium (1.03 g, 44.8 mmol, 50.0 eq.), and DMDS (2.50 mL, 27.8 mmol, 31.0 eq.). The mixture was sonicated to full dissolution of sodium. Biphenyl **31** (200 mg, 0.900 mmol) was added in degassed NMP (1 mL). The apparatus was attached to an emergency

bleach bath. The reaction mixture was stirred at 200 °C for 5 h. Once cooled down to 0 °C, AcCl (4.50 mL, 62.8 mmol, 70.0 eq.) was added. The reaction mixture was stirred at room temperature for 2 h and then poured into an ice-filled separation funnel for extraction with DCM (3 x 20 mL). The combined organic phases were extracted with brine (3 x 50 mL), dried over anhydrous magnesium sulfate, filtered, and evaporated *in vacuo*. Flash chromatography (cyclohexane:DCM 20:80 to 0:100) yielded biphenyl **16** (213 mg, 79 %) as an orange-brown crystalline solid.

M.p.: 81 – 83 °C (DCM).

^{1}H NMR (400 MHz, $CDCl_3$): δ 7.66 – 7.58 (m, 4H), 7.49 (td, *J* = 6.9, 1.6, 2H), 7.41 (dd, *J* = 7.6, 1.5, 2H), 2.45 (s, 6H) ppm.

^{13}C NMR (101 MHz, $CDCl_3$): δ 193.9, 141.4, 133.7, 133.3, 129.8, 128.7, 128.4, 30.4 ppm.

IR ($CHCl_3$): 3087 vw, 3062 vw, 3010 w, 2964 vw, 2927 vw, 1703 vs, 1589 w, 1560 w, 1483 vw, 1464 w, 1424 w, 1390 w, 1383 w, 1354 w, 1300 vw, 1256 vw, 1125 m, 1117 m, 1103 m, 1048 w, 1000 w, 952 m, 888 w, 694 m, 619 m, 524 vw, 435 w cm^{-1}.

UV-Vis ($CHCl_3$): λ_{max} (log ε) = 248 nm (4.78).

ESI MS: 303 ($[M+H]^+$).

HR ESI MS: calculated for $C_{16}H_{15}O_2S_2$ 303.0508, found 303.0507.

5.3 X-ray diffraction

Table 1: Crystallographic data

Compound	**14**	**15**
Formula	$C_{48}H_{34}O_2S_2$	$C_{175}H_{122}O_5S_4$
Molecular weight	706.87	2432.96
Crystal system	triclinic	monoclinic
Space group	*P* -1	*C* 1 2/c 1
a [Å]	9.8013(3)	56.3854(12)
b [Å]	13.5525(4)	11.5352(3)
c [Å]	14.8891(5)	20.0932(4)
α [°]	110.3300(10)	90
β [°]	105.0110(10)	107.8120(10)
γ [°]	93.6410(10)	90
Cell Volume *[Å3]*	1765.36	12442.5(5)
Z	2	4
θ_{max} [°]	27.50	70.1205
Crystal shape	tablet	tablet
Crystal color	yellow	yellow
Dx [g cm^{-3}]	1.330	1.299
R-Factor [%]	3.94	5.53
No. of parameters	496	867

5.4 Solubility data

Table 2: Solubility in mg/mL

Compound	acetone	toluene	DCM
14	13	56	50
33	0.30	1.6	11

5.6 Scanning tunneling microscopy-based break-junction device

Single-molecular electrical conductance of the final [5]helicene **14**, [9]helicene **15**, biphenyl **16** and stilbene **34** was measured with a scanning tunneling microscopy-based break-junction device (Fig. 35) constructed by our group at the Institute of Organic Chemistry and Biochemistry of the Czech Academy of Sciences (IOCB Prague). The device was developed by Dr. Jaroslav Vacek, Dr. Jindřich Nejedlý, Dr. Ladislav Sieger, and Dr. Jana Vacek Chocholoušová (IOCB Prague) in collaboration with experts of fine mechanics engineering and electronics (Prof. Josef Zicha, Czech Technical University in Prague, Faculty of Mechanical Engineering; Prof. Karel Hoffmann, Czech Technical University in Prague, Faculty of Electrical Engineering; BMD a.s.).

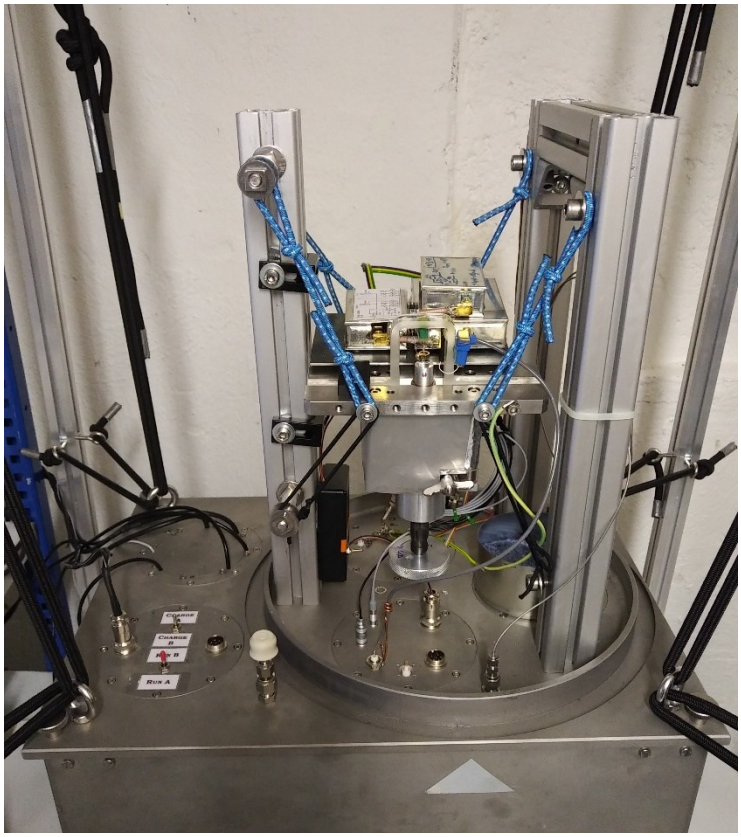

Fig. 35: STM-BJ current setup.

During the measurements**,** the junction was broken at 5 Hz frequency and the data were collected at 50 kSa rate at bias voltage of 0.1 V. The electrical circuit with the stabilized voltage sources (STAB1,2), wave generators (WG), piezo actuators (PZT2, P602), and current-voltage converter (IVC) is shown in Fig. 36. The studied compounds were

measured in mesitylene solutions (10^{-4} M). The measurements were controlled in a software programed in LabView[81] by Dr. Jindřich Nejedlý. The obtained data contained ten thousands of breaking curves and thus required statistical analysis. For this purpose, Fortran[82] analyzing program written by Dr. Jaroslav Vacek (IOCB Prague) was used.

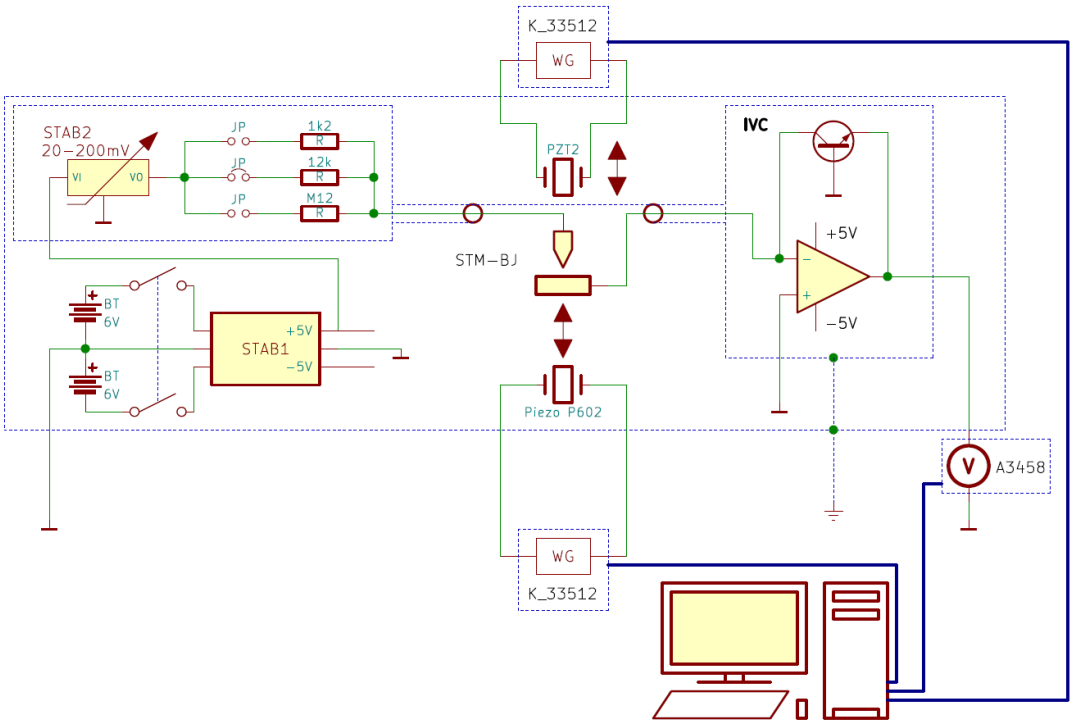

Fig. 36: STM-BJ electrical circuit block scheme.

Tips and cells preparation

The tips were prepared from a high-purity gold wire (125 μm diameter, 99.99%) by electrochemical etching in a KI solution[83] at 6 V potential to form a sharpened gold STM tip as is shown in Fig. 37a. The custom-made glass cells were covered with 200 nm of the high-purity gold (99.99%) in the process of the thermal evaporation in high vacuum (10^{-6} mBar, Fig. 37b). To enable gold deposition on glass, a 10 nm chromium adhesion interlayer was used. All metals were purchased from Goodfellow GmbH.

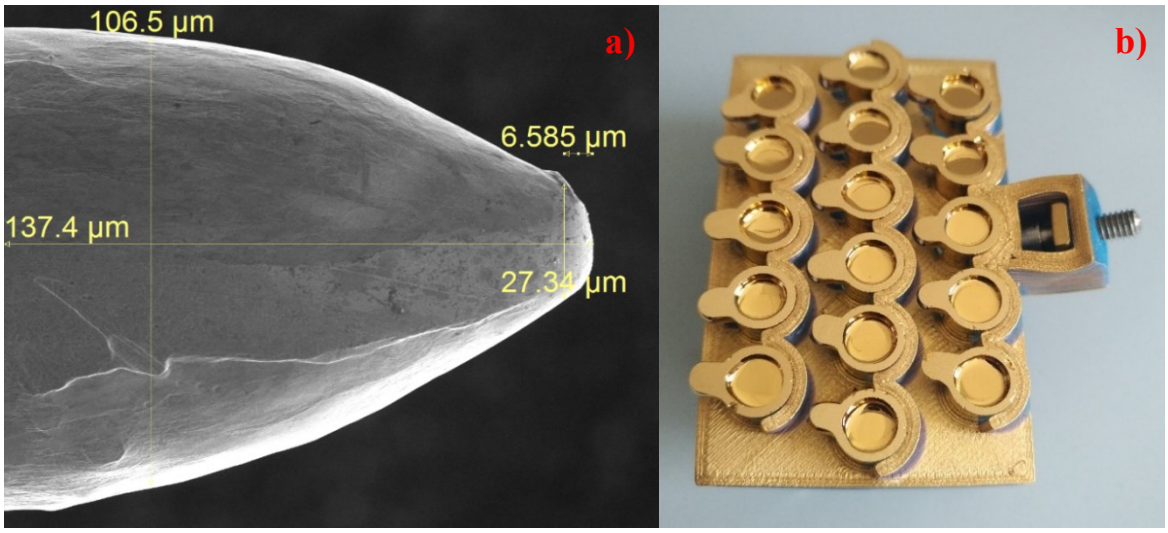

Fig. 37: a) Gold tip and b) glass cells used for STM-BJ experiments.

5.7 Theoretical calculations

The BJ experiments were modelled *in silico* using Non equilibrium Green's function (NEGF) approach[84,85] using periodic semiempirical Slater–Koster tight-binding model as implemented in QuantumWise's Atomistix Toolkit.[71,72,73] First, molecules were optimized at B3LYP/6-31G/GD3 level with Gaussian09[66] ([5]helicene **14,** and [9]helicene **15**, biphenyl **16**, stilbene **34**). The resulting helicene structures were then placed between two gold(111) electrodes using the VNL graphical interface of QuantumWise. The gold-sulfur bond length was set to 2.66 Å[74] and zero bias transmission spectrum, transmission pathways, and transmission eigenstates were then calculated by means of NEGF at semi-empirical DFTB level of theory.

6 Abbreviations

Ac	acetyl
ACN	acetonitrile
AFM	atomic force microscopy
APCI	atmospheric-pressure chemical ionization
bp	base pair
BJ	break-junction
Bu	butyl
CISS	chirality-induced spin selectivity
COSY	correlated spectroscopy
CP-OLED	circularly polarised organic light-emitting diodes
d	doublet
DCM	dichloromethane
dd	doublet of doublet
ddd	doublet of doublet of doublet
DDQ	2,3-dichloro-5,6-dicyano-1,4-benzoquinone
DFT	density functional theory
DFTB	density-functional based tight binding model
DIPA	*N*,*N*-diisopropylamine
DMDS	dimethyl disulfide
DNA	deoxyribonucleic acid
DOS	density of states
dsDNA	double-stranded deoxyribonucleic acid
ECD	electron circular dichroism
ee	enantiomeric excess
EI	electron ionization
EM-BJ	electromigrated break-junction
ESI	electrospray ionization
HR	high resolution
HMBC	heteronuclear multiple bond correlation
HOMO	highest occupied molecular orbital
HOPG	highly oriented pyrolytic graphite
HPLC	high performance liquid chromatography

HSQC	heteronuclear single quantum coherence
IETS	inelastic electron tunneling spectroscopy
IPA	isopropyl alcohol
IR	infrared spectroscopy
LUMO	lowest unoccupied molecular orbital
m (IR)	medium
m (NMR)	multiplet
MC-BJ	mechanically controlled break-junction
mCP-AFM	magnetic conductive probe atomic force microscopy
M.p.	melting point
MS	mass spectrometry
MALDI	matrix assisted laser desorption ionization
NEGF	non equilibrium Green's function
NMP	*N*-methyl-2-pyrrolidone
NMR	nuclear magnetic resonance
Pr	propyl
RT	room temperature
s (IR)	strong
s (NMR)	singlet
sh	shoulder
SP	spin polarization
STM	scanning tunneling microscopy
t	triplet
TBAF	tetrabutylammonium fluoride
td	triplet of doublet
THF	tetrahydrofuran
TMSA	trimethylsilyl acetylene
TOF	time of flight detector
TIPS	triisopropylsilyl
TIPSA	triisopropylsilyl acetylene
TLC	thin-layer chromatography
Tol	*p*-tolyl
TU	Technische Universität
UHV	ultra-high vacuum

vw	very weak
vvw	very very weak
w	weak

7 List of references

1) Newman, M. S.; Hussey, A. S. Optical Activity from a New Type of Steric Hindrance. *J. Am. Chem. Soc.* **1947**, *69*, 978–979.

2) Poater, J.; Visser, R.; Solà, M.; Bickelhaupt, F. M. Polycyclic Benzenoids: Why Kinked Is More Stable than Straight. *J. Org. Chem.* **2007**, *72*, 1134–1142.

3) Newman, M. S.; Lednicer, D. The Synthesis and Resolution of Hexahelicene. *J. Am. Chem. Soc.* **1956**, *78*, 4765–4770.

4) Nakai, Y.; Mori, T.; Inoue, Y. Theoretical and Experimental Studies on Circular Dichroism of Carbo[*n*]Helicenes. *J. Phys. Chem. A* **2012**, *116*, 7372–7385.

5) Vander Donckt, E.; Nasielski, J.; Greenleaf, J. R.; Birks, J. B. Fluorescence of the Helicenes. *Chem. Phys. Lett.* **1968**, *2*, 409–410.

6) Dhbaibi, K.; Abella, L.; Meunier-Della-Gatta, S.; Roisnel, T.; Vanthuyne, N.; Jamoussi, B.; Pieters, G.; Racine, B.; Quesnel, E.; Autschbach, J.; Crassous, J.; Favereau, L. Achieving High Circularly Polarized Luminescence with Push–Pull Helicenic Systems: From Rationalized Design to Top-Emission CP-OLED Applications. *Chem. Sci.* **2021**, *12*, 5522–5533.

7) Yang, Y.; da Costa, R. C.; Fuchter, M. J.; Campbell, A. J. Circularly Polarized Light Detection by a Chiral Organic Semiconductor Transistor. *Nature Photon* **2013**, *7*, 634–638.

8) Sánchez, I. G.; Šámal, M.; Nejedlý, J.; Karras, M.; Klívar, J.; Rybáček, J.; Buděšínský, M.; Bednárová, L.; Seidlerová, B.; Stará, I. G.; Starý, I. Oxahelicene NHC Ligands in the Asymmetric Synthesis of Nonracemic Helicenes. *Chem. Commun.* **2017**, *53*, 4370–4373.

9) Nuckolls, C.; Katz, T. J. Synthesis, Structure, and Properties of a Helical Columnar Liquid Crystal. *J. Am. Chem. Soc.* **1998**, *120*, 9541–9544.

10) Anger, E.; Iida, H.; Yamaguchi, T.; Hayashi, K.; Kumano, D.; Crassous, J.; Vanthuyne, N.; Roussel, C.; Yashima, E. Synthesis and Chiral Recognition Ability of Helical Polyacetylenes Bearing Helicene Pendants. *Polym. Chem.* **2014**, *5*, 4909.

11) Kiran, V.; Mathew, S. P.; Cohen, S. R.; Hernández Delgado, I.; Lacour, J.; Naaman, R. Helicenes – A New Class of Organic Spin Filter. *Adv. Mater.* **2016**, *28*, 1957–1962.

12) Goedicke, Ch.; Stegemeyer, H. Resolution and Racemization of Pentahelicene. *Tetrahedron Lett.* **1970**, *11*, 937–940.

13) Adriaenssens, L.; Severa, L.; Šálová, T.; Císařová, I.; Pohl, R.; Šaman, D.; Rocha, S. V.; Finney, N. S.; Pospíšil, L.; Slavíček, P.; Teplý, F. Helquats: A Facile, Modular, Scalable Route to Novel Helical Dications. *Chem. Eur. J.* **2009**, *15*, 1072–1076.

14) Holmes, D.; Lee, S.; Lotz, S.; Nguyen, S.; Schaller, G.; Schmidt-Radde, R.; Vollhardt, K. (η6-[7]Heliphene)Tricarbonylchromium via an Optimized Preparation of [7]Heliphene. *Synthesis* **2015**, *47*, 2038–2054.

15) Han, S.; Bond, A. D.; Disch, R. L.; Holmes, D.; Schulman, J. M.; Teat, S. J.; Vollhardt, K. P. C.; Whitener, G. D. Total Syntheses and Structures of Angular [6]- and [7]Phenylene: The First Helical Phenylenes (Heliphenes). *Angew. Chem. Int. Ed.* **2002**, *41*, 3223–3227.

16) Meisenheimer, J.; Witte, K. Reduction von 2-Nitronaphtalin. Ber. Dtsch. Chem. Ges. 1903, 36, 4153–4164.

17) Newman, M. S.; Wolf, M. A New Synthesis of Benzo(c)Phenanthrene: L,12-Dimethylbenzo(c)Phenanthrene. *J. Am. Chem. Soc.* **1952**, *74*, 3225-3228.

18) Katz, T. J.; Liu, L.; Willmore, N. D.; Fox, J. M.; Rheingold, A. L.; Shi, S.; Nuckolls, C.; Rickman, B. H. An Efficient Synthesis of Functionalized Helicenes. *J. Am. Chem. Soc.* **1997**, *119*, 10054–10063.

19) Flammang-Barbieux, M.; Nasielski, J.; Martin, R. H. Synthesis of Heptahelicene Benzo[c]phenanthro[4,3-g]phenanthrene. *Tetrahedron Lett.* **1967**, *8*, 743–744.

20) Stará, I. G.; Starý, I. Helically Chiral Aromatics: The Synthesis of Helicenes by [2 + 2 + 2] Cycloisomerization of π-Electron Systems. *Acc. Chem. Res.* **2020**, *53*, 144–158.

21) Martin, R. H.; Baes, H. Helicenes: Photosyntheses of [11], [12] and [14] helicene, *Tetrahedron*, **1975**, *31*, 2135–2137.

22) Gingras, M. One Hundred Years of Helicene Chemistry. Part 1: Non-Stereoselective Syntheses of Carbohelicenes. *Chem. Soc. Rev.* **2013**, *42*, 968–1006.

23) Sudhakar, A.; Katz, T. J. Directive Effect of Bromine on Stilbene Photocyclizations. an Improved Synthesis of [7]Helicene. *Tetrahedron Lett.* **1986**, *27*, 2231–2234.

24) Mori, K.; Murase, T.; Fujita, M. One-Step Synthesis of [16]Helicene. *Angew. Chem.* **2015**, *127*, 6951–6955.

25) Stará, I. G.; Starý, I.; Kollárovič, A.; Teplý, F.; Šaman, D.; Tichý, M. A Novel Strategy for the Synthesis of Molecules with Helical Chirality. Intramolecular [2 + 2 + 2] Cycloisomerization of Triynes under Cobalt Catalysis. *J. Org. Chem.* **1998**, *63*, 4046–4050.

26) Míšek, J.; Teplý, F.; Stará, I. G.; Tichý, M.; Šaman, D.; Císařová, I.; Vojtíšek, P.; Starý, I. A Straightforward Route to Helically Chiral N-Heteroaromatic Compounds: Practical Synthesis of Racemic 1,14-Diaza[5]Helicene and Optically Pure 1- and 2-Aza[6]Helicenes. *Angew. Chem. Int. Ed.* **2008**, *47*, 3188–3191.

27) Chercheja, S.; Klívar, J.; Jančařík, A.; Rybáček, J.; Salzl, S.; Tarábek, J.; Pospíšil, L.; Vacek Chocholoušová, J.; Vacek, J.; Pohl, R.; Císařová, I.; Starý, I.; Stará, I. G. The Use of Cobalt-Mediated Cycloisomerisation of Ynedinitriles in the Synthesis of Pyridazinohelicenes. *Chem. Eur. J.* **2014**, *20*, 8477–8482.

28) Stará, I. G.; Starý, I.; Kollárovič, A.; Teplý, F.; Vyskočil, Š.; Šaman, D. Transition Metal Catalysed Synthesis of Tetrahydro Derivatives of [5]-, [6]- and [7]Helicene. *Tetrahedron Lett.* **1999**, *40*, 1993–1996.

29) Teplý, F.; Stará, I. G.; Starý, I.; Kollárovič, A.; Šaman, D.; Rulíšek, L.; Fiedler, P. Synthesis of [5]-, [6]-, and [7]Helicene via Ni(0)- or Co(I)-Catalyzed Isomerization of Aromatic *Cis*, *Cis*-Dienetriynes. *J. Am. Chem. Soc.* **2002**, *124*, 9175–9180.

30) Jančařík, A.; Rybáček, J.; Cocq, K.; Vacek Chocholoušová, J.; Vacek, J.; Pohl, R.; Bednárová, L.; Fiedler, P.; Císařová, I.; Stará, I. G.; Starý, I. Rapid Access to Dibenzohelicenes and Their Functionalized Derivatives. *Angew. Chem. Int. Ed.* **2013**, *52*, 9970–9975.

31) https://creativecommons.org/licenses/by-sa/2.0/at/legalcode (accessed Jul 28, 2021).

32) Young, R.; Ward, J.; Scire, F. The Topografiner: An Instrument for Measuring Surface Microtopography. *Review of scientific instruments*, **1972**, *43*, 999–1011.

33) Binnig, G.; Rohrer, H.; Gerber, Ch.; Weibel, E. Tunneling through a Controllable Vacuum Gap. *Appl. Phys. Lett.* **1982**, *40*, 178–180.

34) Binnig, G.; Rohrer, H.; Gerber, Ch.; Weibel, E. 7 × 7 Reconstruction on Si(111) Resolved in Real Space. *Phys. Rev. Lett.* **1983**, *50*, 120–123.

35) https://www.nobelprize.org/prizes/physics/1986/summary/ (accessed Jul 28, 2021)

36) Ošťádal, I.; Sobotík, P. Rastrovací tunelovací mikroskopie (STM) a příbuzné techniky. In *Metody analýzy povrchů: iontové, sondové a speciální metody*; Frank, L., Král, J., Eds.; Academia: Praha, 2002; pp 275–295.

37) Low-Current STM Imaging of Self-Assembled 2D Crystals. Oxford Instruments Asylum Research Inc. https://afm.oxinst.com/outreach/application-note-low-current-stm (accessed Jul 28, 2021).

38) Fan, Q.; Wang, C.; Han, Y.; Zhu, J.; Hieringer, W.; Kuttner, J.; Hilt, G.; Gottfried, J. M. Surface-Assisted Organic Synthesis of Hyperbenzene Nanotroughs. *Angew. Chem. Int. Ed.* **2013**, *52*, 4668–4672.

39) Kaliginedi, V.; V. Rudnev, A.; Moreno-García, P.; Baghernejad, M.; Huang, C.; Hong, W.; Wandlowski, T. Promising Anchoring Groups for Single-Molecule Conductance Measurements. *Phys. Chem. Chem. Phys.* **2014**, *16*, 23529–23539.

40) Launay, J.-P.; Verdaguer, M. *Electrons in Molecules*, 1st ed.; Oxford University Press: New York, NY, 2014.

41) Nejedlý, J. The Synthesis of π-Electron Systems Suitable for Transfer and Retention of Charges. PhD Thesis, Charles University: Prague, 2021. Digital Repository. https://dspace.cuni.cz/handle/20.500.11956/124388?locale-attribute=en (accessed Jul 28, 2021).

42) Gehring, P.; Thijssen, J. M.; van der Zant, H. S. J. Single-Molecule Quantum-Transport Phenomena in Break Junctions. *Nat Rev Phys* **2019**, *1*, 381–396.

43) Taniguchi, M.; Tsutsui, M.; Yokota, K.; Kawai, T. Inelastic Electron Tunneling Spectroscopy of Single-Molecule Junctions Using a Mechanically Controllable Break Junction. *Nanotechnology* **2009**, *20*, 434008.

44) Hybertsen, M. S.; Venkataraman, L. Structure–Property Relationships in Atomic-Scale Junctions: Histograms and Beyond. *Acc. Chem. Res.* **2016**, *49*, 452–460.

45) Park, H.; Lim, A. K. L.; Alivisatos, A. P.; Park, J.; McEuen, P. L. Fabrication of Metallic Electrodes with Nanometer Separation by Electromigration. *Appl. Phys. Lett.* **1999**, *75*, 301–303.

46) Šebera, J.; Lindner, M.; Gasior, J.; Mészáros, G.; Fuhr, O.; Mayor, M.; Valášek, M.; Kolivoška, V.; Hromadová, M. Tuning the Contact Conductance of Anchoring Groups in Single Molecule Junctions by Molecular Design. *Nanoscale* **2019**, *11*, 12959–12964.

47) Kaliginedi, V.; V. Rudnev, A.; Moreno-García, P.; Baghernejad, M.; Huang, C.; Hong, W.; Wandlowski, T. Promising Anchoring Groups for Single-Molecule Conductance Measurements. *Phys. Chem. Chem. Phys.* **2014**, *16*, 23529–23539.

48) Su, T. A.; Neupane, M.; Steigerwald, M. L.; Venkataraman, L.; Nuckolls, C. Chemical Principles of Single-Molecule Electronics. *Nat Rev Mater* **2016**, *1*, 16002.

49) Venkataraman, L.; Klare, J. E.; Tam, I. W.; Nuckolls, C.; Hybertsen, M. S.; Steigerwald, M. L. Single-Molecule Circuits with Well-Defined Molecular Conductance. *Nano Lett.* **2006**, *6*, 5.

50) Tsutsui, M.; Taniguchi, M.; Kawai, T. Quantitative Evaluation of Metal−Molecule Contact Stability at the Single-Molecule Level. *J. Am. Chem. Soc.* **2009**, *131*, 10552–10556.

51) Tour, J. M.; Jones, L.; Pearson, D. L.; Lamba, J. J. S.; Burgin, T. P.; Whitesides, G. M.; Allara, D. L.; Parikh, A. N.; Atre, S. Self-Assembled Monolayers and Multilayers of Conjugated Thiols, α,ω.-Dithiols, and Thioacetyl-Containing Adsorbates. Understanding Attachments between Potential Molecular Wires and Gold Surfaces. *J. Am. Chem. Soc.* **1995**, *117*, 9529–9534.

52) Derosa, P. A.; Seminario, J. M. Electron Transport through Single Molecules: Scattering Treatment Using Density Functional and Green Function Theories. *J. Phys. Chem. B* **2001**, *105*, 471–481.

53) Widawsky, J. R.; Darancet, P.; Neaton, J. B.; Venkataraman, L. Simultaneous Determination of Conductance and Thermopower of Single Molecule Junctions. *Nano Lett.* **2012**, *12*, 354–358.

54) Kaneko, S.; Nakazumi, T.; Kiguchi, M. Fabrication of a Well-Defined Single Benzene Molecule Junction Using Ag Electrodes. *J. Phys. Chem. Lett.* **2010**, *1*, 3520–3523.

55) Kim, Y.; Song, H.; Strigl, F.; Pernau, H.-F.; Lee, T.; Scheer, E. Conductance and Vibrational States of Single-Molecule Junctions Controlled by Mechanical Stretching and Material Variation. *Phys. Rev. Lett.* **2011**, *106*, 196804.

56) Ko, C.-H.; Huang, M.-J.; Fu, M.-D.; Chen, C. Superior Contact for Single-Molecule Conductance: Electronic Coupling of Thiolate and Isothiocyanate on Pt, Pd, and Au. *J. Am. Chem. Soc.* **2010**, *132*, 756–764.

57) Kim, T.; Vázquez, H.; Hybertsen, M. S.; Venkataraman, L. Conductance of Molecular Junctions Formed with Silver Electrodes. *Nano Lett.* **2013**, *13*, 3358–3364.

58) Ray, K; Ananthavel, S. P.; Waldeck, D. H.; Naaman, R. Asymmetric Scattering of Polarized Electrons by Organized Organic Films of Chiral Molecules. *Science* **1999**, *283*, 814–816.

59) Naaman, R.; Waldeck, D. H. Spintronics and Chirality: Spin Selectivity in Electron Transport Through Chiral Molecules. *Annu. Rev. Phys. Chem.* **2015**, *66*, 263–281.

60) Kettner, M.; Maslyuk, V. V.; Nürenberg, D.; Seibel, J.; Gutierrez, R.; Cuniberti, G.; Ernst, K.-H.; Zacharias, H. Chirality-Dependent Electron Spin Filtering by Molecular Monolayers of Helicenes. *J. Phys. Chem. Lett.* **2018**, *9*, 2025–2030.

61) Naaman, R.; Paltiel, Y.; Waldeck, D. H. Chirality and Spin: A Different Perspective on Enantioselective Interactions. *chimia (aarau)* **2018**, *72*, 394–398.

62) Gohler, B.; Hamelbeck, V.; Markus, T. Z.; Kettner, M.; Hanne, G. F.; Vager, Z.; Naaman, R.; Zacharias, H. Spin Selectivity in Electron Transmission Through Self-Assembled Monolayers of Double-Stranded DNA. *Science* **2011**, *331*, 894–897.

63) Kettner, M.; Göhler, B.; Zacharias, H.; Mishra, D.; Kiran, V.; Naaman, R.; Fontanesi, C.; Waldeck, D. H.; Sęk, S.; Pawłowski, J.; Juhaniewicz, J. Spin Filtering in Electron Transport Through Chiral Oligopeptides. *J. Phys. Chem. C* **2015**, *119*, 14542–14547.

64) Mondal, P. C.; Kantor-Uriel, N.; Mathew, S. P.; Tassinari, F.; Fontanesi, C.; Naaman, R. Chiral Conductive Polymers as Spin Filters. *Adv. Mater.* **2015**, *27*, 1924–1927.

65) Nejedlý, J.; Šámal, M.; Rybáček, J.; Gay Sánchez, I.; Houska, V.; Warzecha, T.; Vacek, J.; Sieger, L.; Buděšínský, M.; Bednárová, L.; Fiedler, P.; Císařová, I.; Starý, I.; Stará, I. G. Synthesis of Racemic, Diastereopure, and Enantiopure Carba- or Oxa[5]-, [6]-, [7]-, and -[19]Helicene (Di)Thiol Derivatives. *J. Org. Chem.* **2020**, *85*, 248–276.

66) Ing. Arnošt Seidler, unpublished results.

67) Frisch, M. J.; Trucks, G. W.; Schlegel, H. B.; Scuseria, G. E.; Robb, M. A.; Cheeseman, J. R.; Scalmani, G.; Barone, V.; Mennucci, B.; Petersson, G. A.; Nakatsuji, H.; Caricato, M.; Li, X.; Hratchian, H. P.; Izmaylov, A. F.; Bloino, J.; Zheng, G.; Sonnenberg, J. L.; Hada, M.; Ehara, M.; Toyota, K.; Fukuda, R.; Hasegawa, J.; Ishida, M.; Nakajima, T.; Honda, Y.; Kitao, O.; Nakai, H.; Vreven, T.; Montgomery, Jr., J. A.; Peralta, J. E.; Ogliaro, F.; Bearpark, M.; Heyd, J. J.; Brothers, E.; Kudin, K. N.; Staroverov, V. N.; Kobayashi, R.; Normand, J.; Raghavachari, K.; Rendell, A.; Burant, J. C.; Iyengar, S. S.; Tomasi, J.; Cossi, M.; Rega, N.; Millam, J. M.; Klene, M.; Knox,

J. E.; Cross, J. B.; Bakken, V.; Adamo, C.; Jaramillo, J.; Gomperts, R.; Stratmann, R. E.; Yazyev, O.; Austin, A. J.; Cammi, R.; Pomelli, C.; Ochterski, J. W.; Marin, R. L.; Morokuma, K.; Zakrzewski, V. G.; Voth, G. A.; Salvador, P.; Dannenberg, J. J.; Dapprich, S.; Daniels, A. D.; Farkas, Ö.; Foresman, J. B.; Ortiz, J. V.; Cioslowski, J.; Fox, D. J. *Gaussian G09*, Revision E.01; Gaussian, Inc.: Wallingford CT, 2009.

68) Meisner, J. S.; Ahn, S.; Aradhya, S. V.; Krikorian, M.; Parameswaran, R.; Steigerwald, M.; Venkataraman, L.; Nuckolls, C. Importance of Direct Metal−π Coupling in Electronic Transport Through Conjugated Single-Molecule Junctions. *J. Am. Chem. Soc.* **2012**, *134*, 20440–20445.

69) Quek, S. Y.; Kamenetska, M.; Steigerwald, M. L.; Choi, H. J.; Louie, S. G.; Hybertsen, M. S.; Neaton, J. B.; Venkataraman, L. Mechanically Controlled Binary Conductance Switching of a Single-Molecule Junction. *Nature Nanotech* **2009**, *4*, 230–234.

70) Stetsovych, O.; Mutombo, P.; Švec, M.; Šámal, M.; Nejedlý, J.; Císařová, I.; Vázquez, H.; Moro-Lagares, M.; Berger, J.; Vacek, J.; Stará, I. G.; Starý, I.; Jelínek, P. Large Converse Piezoelectric Effect Measured on a Single Molecule on a Metallic Surface. *J. Am. Chem. Soc.* **2018**, *140*, 940–946.

71) Brandbyge, M.; Mozos, J.-L.; Ordejón, P.; Taylor, J.; Stokbro, K. Density-Functional Method for Nonequilibrium Electron Transport. *Phys. Rev. B* **2002**, *65*, 165401.

72) Soler, J. M.; Artacho, E.; Gale, J. D.; García, A.; Junquera, J.; Ordejón, P.; Sánchez-Portal, D. The SIESTA Method for *Ab Initio* Order- *N* Materials Simulation. *J. Phys. Condens. Matter* **2002**, *14*, 2745–2779.

73) *QuantumATK 2020.09*; Synopsys Corporate: Mountain View, CA, 2020.

74) Zhou, Q.; Yamada, A.; Feng, Q.; Hoskins, A.; Dunietz, B. D.; Lewis, K. M. Modification of Molecular Conductance by in Situ Deprotection of Thiol-Based Porphyrin. *ACS Appl. Mater. Interfaces* **2017**, *9*, 15901–15906.

75) He, J.; Chen, F.; Li, J.; Sankey, O. F.; Terazono, Y.; Herrero, C.; Gust, D.; Moore, T. A.; Moore, A. L.; Lindsay, S. M. Electronic Decay Constant of Carotenoid Polyenes from Single-Molecule Measurements. *J. Am. Chem. Soc.* **2005**, *127*, 1384–1385.

76) Sheldrick, G. M. *SHELXT* – Integrated Space-Group and Crystal-Structure Determination. *Acta Crystallogr. Sect. Found. Adv.* **2015**, *71*, 3–8.

77) Sheldrick, G. M. Crystal Structure Refinement with *SHELXL*. *Acta Crystallogr. Sect. C Struct. Chem.* **2015**, *71*, 3–8.

78) Naveen, K.; Perumal, P. T.; Cho, D.-H. Domino Palladium-Catalyzed Double Norbornene Insertion/Annulation Reaction: Expeditious Synthesis of Overcrowded Tetrasubstituted Olefins. *Org. Lett.* **2019**, *21*, 4350–4354.

79) Shinde, P. S.; Shaikh, A. C.; Patil, N. T. Efficient Access to Alkynylated Quinalizinones via the Gold(I)-Catalyzed Aminoalkynylation of Alkynes. *Chem. Commun.* **2016**, *52*, 8152–8155.

80) Liu, Y.; Bergès, J.; Zaid, Y.; Chahdi, F. O.; Van Der Lee, A.; Harakat, D.; Clot, E.; Jaroschik, F.; Taillefer, M. Aerobic and Ligand-Free Manganese-Catalyzed Homocoupling of Arenes or Aryl Halides via in Situ Formation of Aryllithiums. *J. Org. Chem.* **2019**, *84*, 4413–4420.

81) LabView – National Instruments https://www.ni.com/en-us/shop/labview.html (accessed Jul 28, 2021).

82) Fortran Programming Language; 2015.

83) Hu, Z.; Ritzdorf, T. Cyanide- and Thiourea-Free Electrochemical Etching of Gold for Microelectronics Applications. *J. Electrochem. Soc.* **2007**, *154*, D543.

84) Stokbro, K.; Taylor, J.; Brandbyge, M.; Guo, H. Ab-Initio Non-Equilibrium Green's Function Formalism for Calculating Electron Transport in Molecular Devices. In *Introducing Molecular Electronics*; Cuniberti, G., Richter, K., Fagas, G., Eds.; Springer Berlin Heidelberg, **2006**, 117–151.

85) Koentopp, M.; Chang, C.; Burke, K.; Car, R. Density Functional Calculations of Nanoscale Conductance. *J. Phys. Condens. Matter* **2008**, *20*, 083203.